

## MOJAVE XII: ACCELERATION AND COLLIMATION OF BLAZAR JETS ON PARSEC SCALES

D. C. HOMAN<sup>1</sup>, M. L. LISTER<sup>2</sup>, Y. Y. KOVALEV<sup>3,4</sup>, A. B. PUSHKAREV<sup>5,6,4</sup>, T. SAVOLAINEN<sup>4,7</sup>, K. I. KELLERMANN<sup>8</sup>, J. L. RICHARDS<sup>2</sup>, AND E. ROS<sup>4,9,10</sup>

*Accepted for publication in The Astrophysical Journal.*

### ABSTRACT

We report on the acceleration properties of 329 features in 95 blazar jets from the MOJAVE VLBA program. Nearly half the features and three-quarters of the jets show significant changes in speed and/or direction. In general, apparent speed changes are distinctly larger than changes in direction, indicating that changes in the Lorentz factors of jet features dominate the observed speed changes rather than bends along the line of sight. Observed accelerations tend to increase the speed of features near the jet base,  $\lesssim 10 - 20$  parsecs projected, and decrease their speed at longer distances. The range of apparent speeds at fixed distance in an individual jet can span a factor of a few, indicating that shock properties and geometry may influence the apparent motions; however, we suggest that the broad trend of jet features increasing their speed near the origin is due to an overall acceleration of the jet flow out to de-projected distances of order  $10^2$  parsecs, beyond which the flow begins to decelerate or remains nearly constant in speed. We estimate intrinsic rates of change of the Lorentz factors in the galaxy frame of order  $\dot{\Gamma}/\Gamma \simeq 10^{-3}$  to  $10^{-2}$  per year which can lead to total Lorentz factor changes of a factor of a few on the length scales observed here. Finally, we also find evidence for jet collimation at projected distances of  $\lesssim 10$  parsecs in the form of the non-radial motion and bending accelerations that tend to better align features with the inner jet.

*Keywords:* galaxies : active — galaxies : jets — radio continuum : galaxies — quasars : general — BL Lacertae objects : general — surveys

### 1. INTRODUCTION

The National Radio Astronomy Observatory's Very Long Baseline Array (VLBA)<sup>11</sup> has revolutionized the study of powerful extragalactic radio jets associated with Active Galactic Nuclei (AGNs) by allowing highly sensitive, regular observations of the parsec-scale structure and polarization of large samples. The extraordinary resolution of the VLBA combined with the extreme time compression created by highly relativistic motion beamed along our line of sight allows study on a human timescale of physical processes spanning centuries in the host galaxy:  $\Delta t_{\text{obs}} = (1+z)(1-\beta \cos\theta)\Delta t$ , where  $\Delta t_{\text{obs}}$  is the observed time interval,  $\Delta t$  is the time in the host

galaxy,  $\beta$  is the speed of the moving jet feature in units of the speed of light, and  $\theta$  is the angle the jet feature makes to our line of sight. This ability to directly observe long timescale processes over the span of a decade is essential for addressing long standing questions about the formation, acceleration, and collimation of AGN jets from the supermassive black hole/accretion disk system (e.g. Meier et al. 2001; Vlahakis & Königl 2004; Sikora et al. 2005; Komissarov 2011).

In recent years, Very Long Baseline Interferometry (VLBI) monitoring programs of the parsec-scale structure of powerful extragalactic radio jets have begun to span long enough *time* baselines to directly study the apparent acceleration of large numbers of individual jet features across many jets (Lister et al. 2009b; Homan et al. 2009; Piner et al. 2012). These works extend earlier studies of acceleration in individual jets (e.g. Wardle et al. 1994; Zensus et al. 1995; Gómez et al. 2001; Homan et al. 2003; Jorstad et al. 2004; Savolainen et al. 2006a) or small numbers of jets (Homan et al. 2001; Jorstad et al. 2005; Piner et al. 2007) to allow statistical analysis of the patterns in observed acceleration. The MOJAVE program<sup>12</sup> (e.g. Lister & Homan 2005; Lister et al. 2009a) is a continuation of the 2cm Survey (Kellermann et al. 1998, 2004; Zensus et al. 2002; Kovalev et al. 2005), and together they form the longest running VLBI astrophysical monitoring program with continuous observations of many jets. To date, eleven survey papers have been published in the MOJAVE series. Our most recent kinematics results were presented by Lister et al. (2013, hereafter Paper X) for 887 moving features in 200 AGN jets based

<sup>1</sup> Department of Physics, Denison University, Granville, OH 43023; homand@denison.edu

<sup>2</sup> Department of Physics, Purdue University, 525 Northwestern Avenue, West Lafayette, IN 47907, USA;

<sup>3</sup> Astro Space Center of Lebedev Physical Institute, Profsoyuznaya 84/32, 117997 Moscow, Russia;

<sup>4</sup> Max-Planck-Institut für Radioastronomie, Auf dem Hügel 69, 53121 Bonn, Germany;

<sup>5</sup> Pulkovo Observatory, Pulkovskoe Chaussee 65/1, 196140 St. Petersburg, Russia;

<sup>6</sup> Crimean Astrophysical Observatory, 98409 Nauchny, Crimea, Ukraine;

<sup>7</sup> Aalto University Metsähovi Radio Observatory, Metsähovintie 114, 02540 Kylmälä, Finland;

<sup>8</sup> National Radio Astronomy Observatory, 520 Edgemont Road, Charlottesville, VA 22903, USA;

<sup>9</sup> Observatori Astronòmic, Universitat de València, Parc Científic, C. Catedrático José Beltrán 2, E-46980 Paterna, València, Spain

<sup>10</sup> Departament d'Astronomia i Astrofísica, Universitat de València, C. Dr. Moliner 50, E-46100 Burjassot, València, Spain

<sup>11</sup> The National Radio Astronomy Observatory is a facility of the National Science Foundation operated under cooperative agreement by Associated Universities, Inc.

<sup>12</sup> <http://www.astro.purdue.edu/MOJAVE/>

on observations spanning the period from 1994 Aug 31 to 2011 May 1. Paper X updated our earlier kinematic and acceleration results presented in Lister et al. (2009b, hereafter Paper VI) and Homan et al. (2009, hereafter Paper VII), extended our time baseline by four years, increased our sample of jet features by nearly 70%, and examined changes in jet position angle over time and the dispersion in jet feature speed within individual jets.

In this paper, we analyze observed accelerations for the kinematic results presented in Paper X. This work extends the analysis developed in Paper VII by expanding our sample of high quality motions suitable for detailed acceleration study from 203 features in 63 jets to 329 features in 95 jets. We study both *parallel* accelerations, along the direction of motion, and *perpendicular* accelerations that change the direction of motion; however, we focus particular attention on the relationship between parallel acceleration and distance from the base of the jet. Paper VII reported that jet features tend to accelerate at short projected distances but decelerate at large distances, suggesting that the jet flow was speeding up near the base and decelerating further out, with a transition region in the range  $\sim 15$  pc. In their analysis of ten years of observations performed by the global VLBI array for astrometry and geodesy (Petrov et al. 2009), Piner et al. (2012) confirmed the preponderance of positive accelerations found at short distances but could not confirm the switch to a preponderance of decelerations at larger distances from the core since their sample had too few jet features beyond 15 pc. In addition to revisiting this relationship with much improved data, we also examine directly the relationship between apparent speed and jet distance through the use of *speed profiles* predicted from the acceleration kinematics fits, and we discuss the implications for changes in the jet Lorentz factor on parsec scales.

This paper is organized as follows: Section 2 reviews the relationship between observed accelerations and intrinsic changes in speed and direction of parsec scale jet features. The sample of jet features studied for acceleration is described in section 3, where we also report the results of our analysis of these data. Section 4 presents a discussion of these results, and our conclusions appear in §5. Throughout this paper we assume a cosmology with  $H_0 = 71 \text{ km s}^{-1} \text{ Mpc}^{-1}$ ,  $\Omega_\Lambda = 0.73$ , and  $\Omega_M = 0.27$  (Hinshaw et al. 2009).

## 2. ACCELERATED MOTION

Here we summarize relationships describing changes in apparent speed of parsec-scale AGN jet features and how those apparent changes relate to changes in intrinsic properties of the jet. More detailed discussion and derivations of these expressions are given in Paper VII.

The apparent speed on the 2-D sky plane for a jet feature or pattern moving with intrinsic speed  $\beta$  at angle  $\theta$  to the line of sight is given by the following familiar expression:

$$\beta_{\text{app}} = \frac{\beta \sin \theta}{1 - \beta \cos \theta}. \quad (1)$$

The intrinsic velocity,  $\vec{\beta}$ , is a vector which can change in speed and/or direction, resulting in apparent changes to the motion in the 2-D sky plane. We characterize

these apparent changes as accelerations either *parallel* or *perpendicular* to the apparent velocity:

$$\dot{\beta}_{\parallel \text{app}} = \frac{d\beta_{\parallel \text{app}}}{dt_{\text{app}}} = \frac{\dot{\beta} \sin \theta + \beta \dot{\theta} (\cos \theta - \beta)}{(1 - \beta \cos \theta)^3} \quad (2)$$

and

$$\dot{\beta}_{\perp \text{app}} = \frac{d\beta_{\perp \text{app}}}{dt_{\text{app}}} = \frac{\beta \dot{\phi} \sin \theta}{(1 - \beta \cos \theta)^2}, \quad (3)$$

where  $\dot{\beta}$ ,  $\dot{\theta}$ , and  $\dot{\phi}$  are the intrinsic rates of change of the jet feature’s speed, angle to the line of sight, and azimuthal angle of the component’s motion respectively. Note that the intrinsic velocity vector angles,  $\theta$  and  $\phi$ , are as defined in Figure A1 of Paper VII, and that  $\phi$  corresponds directly to observed proper motion vector direction for jet features given in §3.

From these expressions, it is clear that parallel accelerations, i.e. speeding up or slowing down along the apparent velocity vector, can be generated *either* by changes in the intrinsic speed,  $\beta$ , *or* by changes in the angle to the line of sight,  $\theta$ , or both. Determining the extent to which intrinsic speed changes can explain the observed accelerations is crucial to their physical interpretation. If all of the observed parallel accelerations are due only to intrinsic changes in speed, at any given time the relative rate of change of the Lorentz factor,  $\Gamma = 1/\sqrt{1 - \beta^2}$ , is given by the following expression (Paper VII):

$$\frac{\dot{\Gamma}}{\Gamma} = \frac{\beta^2 \dot{\beta}_{\parallel \text{app}}}{\delta^2 \beta_{\text{app}}} \quad (4)$$

where  $\delta$  is the Doppler factor:  $\delta = 1/(\Gamma(1 - \beta \cos \theta))$ .

However, if all the intrinsic changes are changes in direction only, i.e. “bending” of the component trajectory, then apparent parallel accelerations should usually be accompanied by apparent perpendicular accelerations. Indeed, we can use the relative magnitudes of the parallel and perpendicular accelerations to draw statistical conclusions about the prevalence of intrinsic changes in speed in our sample. Paper VII showed that for a parsec-scale flux-density limited sample, like MOJAVE, the parallel accelerations should only be about 60% of the magnitude of the perpendicular accelerations when averaged across the sample if the observed accelerations are due only to intrinsic changes in direction of motion.

## 3. DATA AND RESULTS

Paper X presented parsec-scale kinematics results for 887 moving features in 200 AGN jets, including acceleration fits for 557 features with 10 or more epochs of observation. Here we analyze the apparent accelerations of jet features both parallel,  $\dot{\mu}_{\parallel}$ , and perpendicular,  $\dot{\mu}_{\perp}$ , to their observed proper motion vector,  $\vec{\mu}$ . As in our original acceleration analysis in Paper VII, we restrict the sample for this paper to those having a proper motion,  $\mu$ , of at least  $3\sigma$  significance, a known redshift (required for relative acceleration analysis, see below), and an uncertainty of no more than  $5^\circ$  in the misalignment between the average position angle of the feature over time,  $\langle \vartheta \rangle$ , and the direction of its proper motion vector,  $\phi$ . This last condition guarantees that the meaning of

**Table 2**  
Statistics of Acceleration Sample

Property	Value
Number Jet Features	329
Number of $\geq 3\sigma$ Parallel Accelerations	123
Number of $\geq 3\sigma$ Perpendicular Accelerations	76
Mean Magnitude of Relative Parallel Accel.	$0.233 \text{ yr}^{-1}$
Median Magnitude of Relative Parallel Accel.	$0.130 \text{ yr}^{-1}$
Mean Magnitude of Relative Perp. Accel.	$0.115 \text{ yr}^{-1}$
Median Magnitude of Relative Perp. Accel.	$0.071 \text{ yr}^{-1}$
Number of High Parallel Accel. ( $ \dot{\eta}_{\parallel}  - 2\sigma > 0.1$ )	85
Number of Low Parallel Accel. ( $ \dot{\eta}_{\parallel}  + 2\sigma \leq 0.1$ )	54
Number of High Perp. Accel. ( $ \dot{\eta}_{\perp}  - 2\sigma > 0.1$ )	34
Number of Low Perp. Accel. ( $ \dot{\eta}_{\perp}  + 2\sigma \leq 0.1$ )	83
Number of $\geq 3\sigma$ Non-radial Motions	156
Number of Non-radial Motions with $ \langle\vartheta\rangle - \phi  \geq 10^\circ$	87

“parallel” and “perpendicular”, defined relative to the observed proper motion vector, is unambiguous. Applying these criteria yields a sample of 329 features in 95 jets suitable for the analysis in this paper, and they are listed in Table 1, along with a summary of their kinematic properties. Paper X includes the full proper motion results, along with plots of their motion, for all of these features.<sup>13</sup> It is important to note that we can only confidently measure and compare the acceleration properties of the well defined, long lived features meeting the criteria described above and in Paper X. Jets also exhibit complex behavior, including stationary and transitory features, that may not be captured by the features suitable for acceleration study. We include discussion of the complexities in deducing the jet flow behavior from observed features in §4.1.2.

To compare accelerations of jet features with different apparent speeds, we use their relative accelerations as defined in Paper VII:

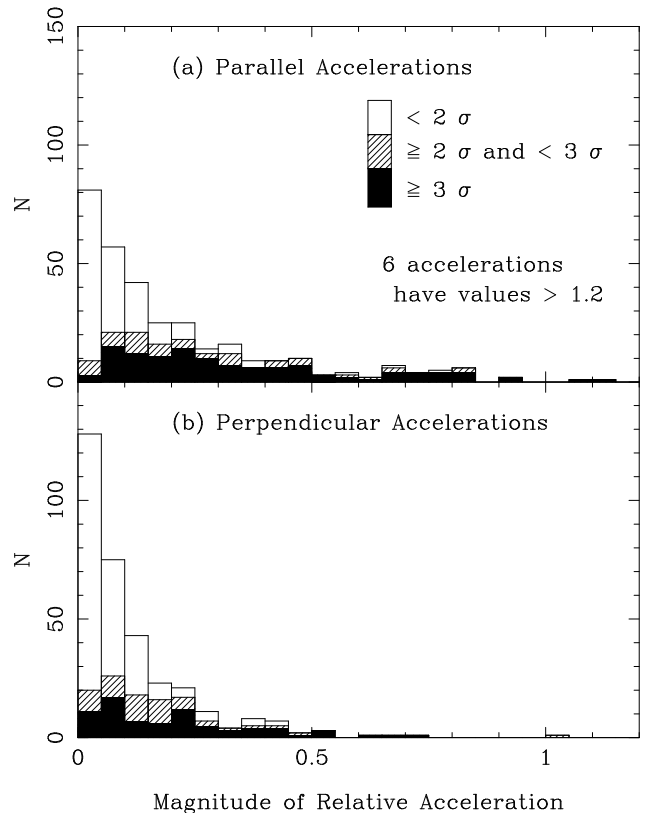
$$\dot{\eta}_{\parallel} = \dot{\beta}_{\parallel \text{app}} / \beta_{\text{app}} = (1+z)\dot{\mu}_{\parallel} / \mu, \quad (5)$$

and

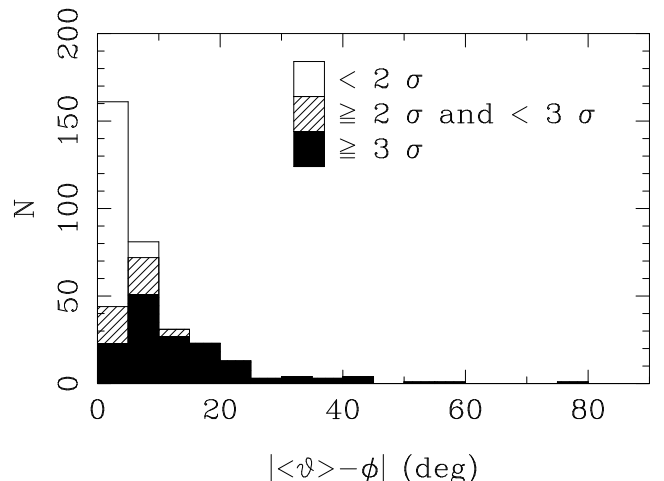
$$\dot{\eta}_{\perp} = \dot{\beta}_{\perp \text{app}} / \beta_{\text{app}} = (1+z)\dot{\mu}_{\perp} / \mu. \quad (6)$$

Table 2 summarizes the properties of the acceleration sample as a whole, and the distributions of the parallel and perpendicular relative accelerations are plotted in Figure 1. More than one-third (37%) of the jet features in our sample have significant ( $\geq 3\sigma$ ) parallel accelerations, indicating a change in apparent speed, and nearly a quarter (23%) have significant perpendicular accelerations, indicating a change in direction of apparent motion. Altogether, one-half (50%) of the jet features have one or both kinds of acceleration at the  $\geq 3\sigma$  level, and three-quarters of the 95 jets we studied have at least one feature with significant acceleration. In general, parallel accelerations are distinctly larger than perpendicular accelerations, and a Kolmogorov-Smirnov (K-S) test gives a probability  $P < 10^{-7}$  ( $N = 329$ ) that they are drawn from the same distribution. The typical magnitude of the

<sup>13</sup> Paper X does not report an apparent speed or relative accelerations for 0716+714 due to a lack of a spectroscopic redshift. Here we compute results for 0716+714 using the redshift estimate,  $z = 0.31 \pm 0.08$  by Nilsson et al. (2008) based on host galaxy magnitude. Using a different value in the range,  $z = 0.2315 - 0.322$  given by Danforth et al. (2013) would not change our acceleration results appreciably.



**Figure 1.** Histograms of magnitudes of relative accelerations, parallel,  $\dot{\eta}_{\parallel}$  (panel (a)), and perpendicular,  $\dot{\eta}_{\perp}$  (panel (b)), to the proper motion vector direction. Hash and solid fill styles indicate angular acceleration significant at the  $2-3\sigma$  and  $\geq 3\sigma$  levels, respectively. As indicated, six parallel accelerations lie to the right of the boundary of panel (a).



**Figure 2.** Histogram of the magnitude of the proper motion misalignment angle,  $|\langle\vartheta\rangle - \phi|$ . Hash and solid fill styles indicate non-radial motions significant at the  $2-3\sigma$  and  $\geq 3\sigma$  levels respectively. Three jet features had misalignment angles  $\geq 90^\circ$  and do not appear in the plot.

observed parallel accelerations is nearly a factor of two larger than the perpendicular accelerations, irrespective of whether the means or the medians are used.

In addition to the directly observed accelerations, we measure the non-radial motion of jet features, comparing their mean structural position angle,  $\langle\vartheta\rangle$ , to their proper

motion vector direction,  $\phi$ . Non-radial features have a proper motion vector that does not point back to the jet core (see the next subsection). Figure 2 is a histogram of these observed mis-alignments. Nearly half of our sample (47%) has motion that is significantly non-radial, and one-quarter (26%) of the motions are mis-aligned by  $10^\circ$  or more.

### 3.1. Parallel Acceleration vs. Jet Distance

As we explore in §4, the distinctly larger magnitudes of parallel accelerations as compared to perpendicular accelerations indicate that the observed parallel accelerations are more likely to reflect intrinsic changes in the Lorentz factor of propagating features than changes in their angle to the line of sight. In this section we explore the relationship between significant ( $\geq 3\sigma$ ) parallel accelerations and distance of the feature from the observed base of the jet or “core”.<sup>14</sup>

Figure 3 plots the magnitude of positive (blue) and negative (red) parallel accelerations as a function of angular distance along the jet in panels (a) and (b). Panel (a) plots the measured *angular* accelerations,  $\dot{\mu}_{\parallel}$ , directly, and panel (b) plots the *relative* accelerations,  $\dot{\eta}_{\parallel}$ , as defined in equation 5. In panel (b), there appears to be a trend of decreasing relative accelerations with increasing angular separation up to about  $\langle R \rangle \simeq 2$  milli-arcsec; however, this is an artifact of calculating relative acceleration by dividing out the average angular speed,  $\mu$ . Jet features at small average angular separation must have a small  $\mu \leq 2\langle R \rangle / \Delta t_{obs}$ , where  $\Delta t_{obs}$  is the time span of our observations. To be measured at the three sigma level, they must have a relative acceleration at least  $\dot{\eta}_{\parallel} \gtrsim 3\sigma \Delta t_{obs} / 2\langle R \rangle$  where  $\sigma$  is the uncertainty in the measured angular acceleration. Median values for the quantities are  $\sigma = 0.0135 \text{ mas yr}^{-2}$  and  $\Delta t_{obs} = 7.5$  years, and the dotted line in panel (b) shows our approximate measurement threshold using these median values. Individual measurements may have smaller values of these quantities separately, but their product,  $\sigma \Delta t_{obs}$ , is  $> 0.032 \text{ mas yr}^{-1}$  in 90% of the jet features we studied, and the dashed line in panel (b) gives a more conservative threshold using this value.

We note that this inability to measure small *relative* accelerations at small angular distances may affect our interpretation of the magnitude of the acceleration at small distances. Panel (c) of Figure 3 plots relative accelerations versus projected linear distance, and we have marked with solid circles those features with  $\langle R \rangle \geq 2.0$  mas to help assess the degree to which features at small projected linear distance are dominated by measurements made at small angular distance. There is a thorough mix of features at all projected distances out to  $\simeq 15$  pc. In our subsequent discussion of the *magnitude* of relative acceleration versus projected linear distance, we will try to mitigate any bias due to this effect by also averaging all measured acceleration values, even if they fall below the  $3\sigma$  limit; however, the primary results discussed below are related to the *sign* of

<sup>14</sup> We note that NGC 1052 (0238-084) at a redshift of just 0.005 is significantly closer than the other jets in this sample and has projected linear distances an order of magnitude smaller. We exclude NGC 1052 jet features at  $< 1$  parsec from the plots in this section to allow a clearer view of the bulk of the sample, but they are included in our statistics.

the parallel acceleration as a function of distance, and those results are unaffected.

As found in Paper VII, there is no apparent relationship between the sign of the acceleration and *angular* distance. We detect no difference between the angular distance distributions of positive and negative parallel accelerations with a K–S test ( $P = 0.32$ ,  $N_+ = 66$ ,  $N_- = 57$ ). However, there is clearly a relationship with projected *linear* distance, plotted in panel (c) of Figure 3. Jet features are more likely to show positive parallel acceleration (speeding up) near the base of the jet and negative parallel acceleration (slowing down) at larger linear distances from the core. A K–S test shows a probability  $P = 6 \times 10^{-6}$  ( $N_+ = 66$ ,  $N_- = 57$ ) that the distances of the positive and negative accelerations are drawn from the same distribution. The mean projected distances for the positive and negative accelerations are 9.0 pc and 22.5 pc respectively. It is important to note that for a parsec-scale flux-density limited sample, such as MOJAVE, the range of angles to the line of sight isn’t large (with the exception of the handful of radio galaxies at low redshift); therefore, any intrinsic trends with distance are not likely to be smeared out by differing jet orientations (Lister & Marscher 1997).

While we argue above and in §4 that *on average* intrinsic changes in Lorentz factor make a larger contribution to the observed parallel accelerations than changes in their angle to the line of sight, we do not know for any individual feature which type of intrinsic change makes the larger contribution. Observed perpendicular accelerations do give us an indication; however, as we expect that large parallel accelerations due solely to jet bending would be typically accompanied by large perpendicular accelerations as it is unlikely the bend will be entirely along our line of sight and changes outside of our line of sight are greatly magnified due to projection. Thus we expect that if we plot only the parallel accelerations for jet features with a large parallel/perpendicular acceleration ratio, we would be more likely to see the effect of Lorentz factor changes than changes to the line of sight.

Figure 4 plots parallel acceleration versus projected linear distance for all the features with a parallel/perpendicular ratio  $\geq 2.0$  in panel (a) and all of those with a ratio  $< 2.0$  in panel (b). Our expectation is confirmed, as we clearly see a strong relationship between sign of the parallel acceleration and projected linear distance in panel (a) but not in panel (b). For the jet features with a parallel/perpendicular ratio  $\geq 2.0$ , a K–S test shows a probability  $P = 2 \times 10^{-6}$  ( $N_+ = 49$ ,  $N_- = 39$ ) that the distances of the positive and negative accelerations are drawn from the same distribution. The mean distances for the positive and negative accelerations are 8.3 pc and 25.1 pc respectively. For jet features with a parallel/perpendicular ratio  $< 2.0$ , a K–S test detects no significant difference in their distance distributions ( $P = 0.57$ ,  $N_+ = 17$ ,  $N_- = 18$ ) with means of 11.0 and 16.9 pc for positive and negative accelerations, respectively.

Figure 5 is a plot of the jet features in Figure 4(a) broken into low redshift,  $z < 0.5$  (panel a), and high redshift,  $z \geq 0.5$  (panel b). The difference between positive and negative accelerations shows up in the same manner for both low and high redshift sources and is significant in

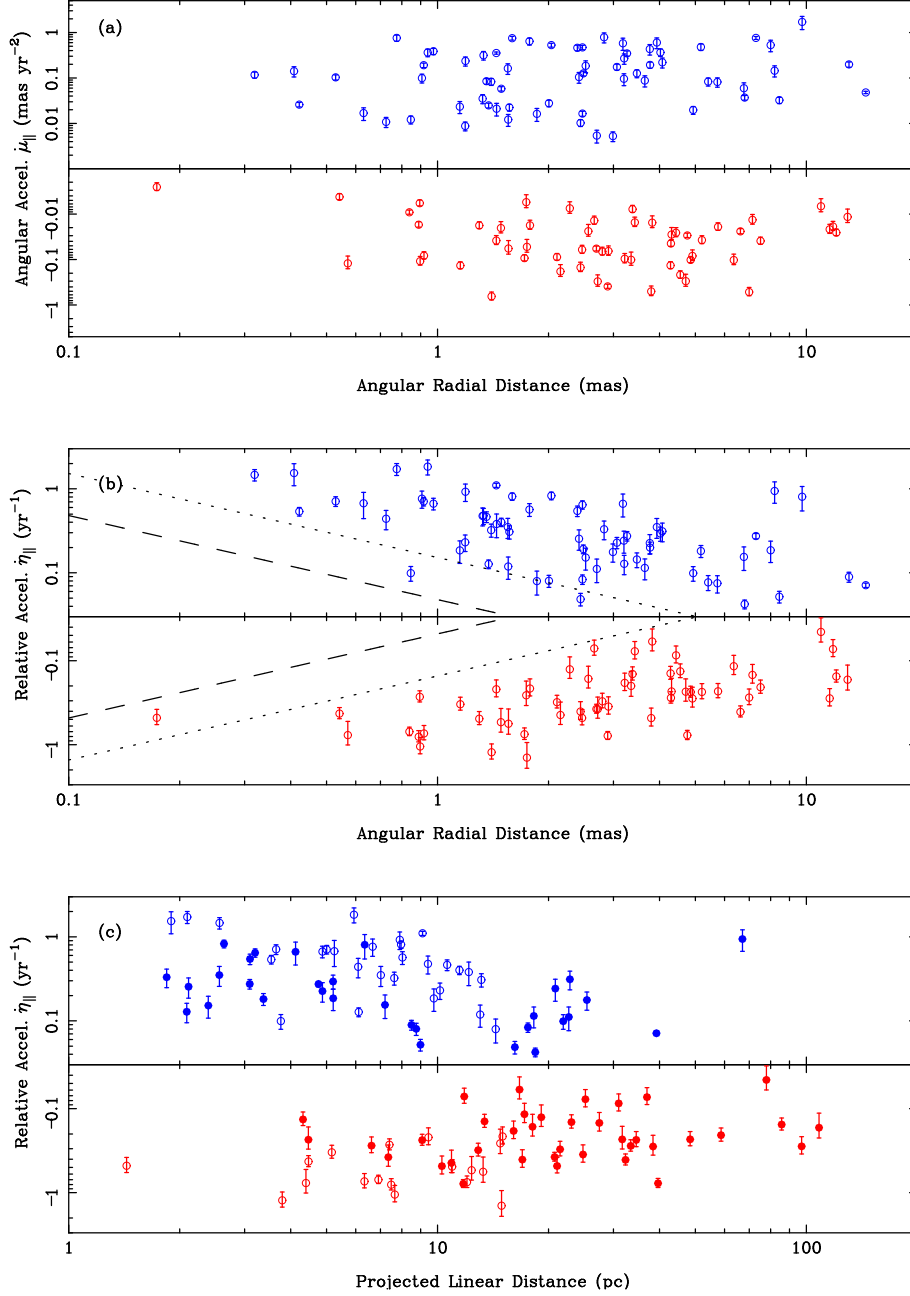


**Figure 3.** Panels (a) and (b) plot significant parallel accelerations ( $\geq 3\sigma$ ) against average angular distance from the core position in milli-arcseconds. Panel (a) plots measured angular acceleration,  $\dot{\mu}_{\parallel}$ , and panel (b) plots relative parallel acceleration,  $\dot{\eta}_{\parallel}$ . The dashed and dotted lines in panel (b) indicate estimates for our threshold for measuring large relative accelerations at small angular distance, see §3.1. Panel (c) plots relative parallel acceleration versus projected linear distance in parsecs. The solid points indicate features at angular distances  $\geq 2.0$  milli-arcseconds. Note that in panel (c), eight features from NGC 1052 at projected linear distances  $< 1.0$  pc are not plotted for clarity; seven of these have positive acceleration, and one has negative.

both cases:  $P = 0.003$  ( $N_+ = 33, N_- = 12$ ) and  $P = 0.01$  ( $N_+ = 16, N_- = 27$ ), respectively.

To further evaluate the relationship between parallel acceleration and projected distance, histograms of the distances in Figure 4(a) are given in the first two panels of Figure 6. Panel (c) of Figure 6 is a histogram of projected distances for features with no apparent parallel or perpendicular acceleration. The distance histogram of features with no apparent acceleration is similar to the distance histogram for features with negative parallel acceleration, but both clearly differ from the histogram of

features with positive parallel acceleration. The bottom panel, (d), of Figure 6 shows the average relative parallel acceleration in each distance bin for the features plotted in the three histograms above. The average relative acceleration decreases with distance from large positive values at very short projected distances to progressively smaller averages, until the average acceleration switches sign beyond 10 pc, where it takes on modest values up to  $-0.2 \text{ yr}^{-1}$ .

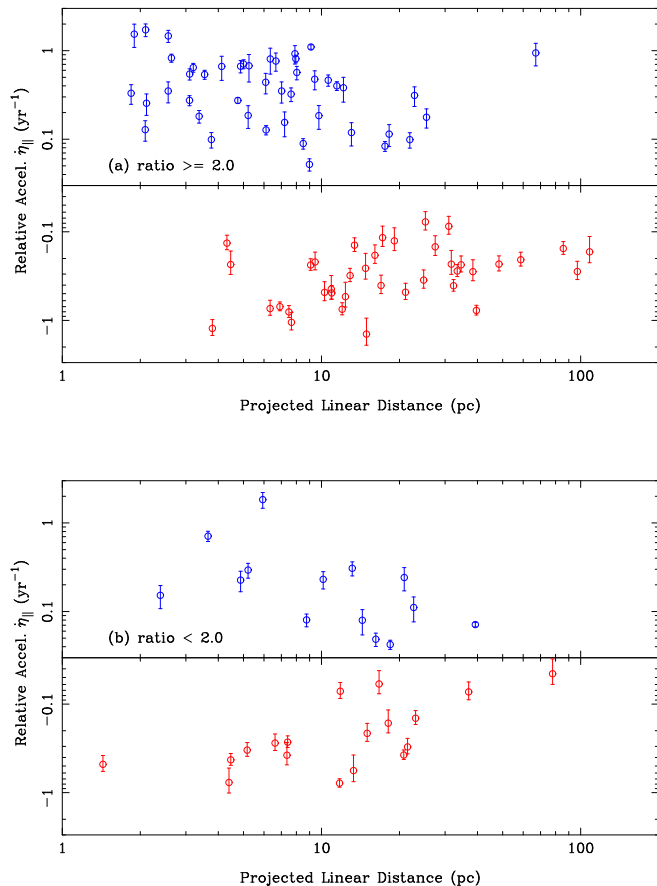


**Figure 4.** Relative parallel accelerations,  $\dot{\eta}_{\parallel}$  for all jet features with  $\geq 3\sigma$  parallel accelerations plotted against average projected linear distance from the core position in parsecs. Features with parallel to perpendicular acceleration ratios of  $\geq 2.0$  are plotted in panel (a), and features with ratios  $< 2.0$  are plotted in panel (b). Eight features from NGC 1052 at projected distances  $< 1.0$  pc do not appear in the plots for clarity; seven of those have positive acceleration, and one has negative.

### 3.2. Perpendicular Acceleration vs. Proper Motion Mis-alignment

Here we explore the relationship between observed perpendicular acceleration and apparent mis-alignment between the proper motion vector direction,  $\phi$ , and the mean structural position angle of the jet feature,  $\langle \vartheta \rangle$ . Jet features that have a significant mis-alignment between their proper motion vector and structural position angle have non-ballistic motion, and therefore, we expect that they have experienced perpendicular accelerations that have changed their trajectory since being ejected from the base of the jet.

Figure 7 shows histograms of the magnitude of the proper motion mis-alignment with respect to the mean structural position angle of the jet feature for two types of jet features. Panel (a) includes features with small perpendicular accelerations,  $|\dot{\eta}_{\perp}| + 2\sigma \leq 0.1$ , and Panel (b) includes features with large perpendicular accelerations,  $|\dot{\eta}_{\perp}| - 2\sigma > 0.1$ . The two distributions clearly differ ( $P < 10^{-8}$ ) with large perpendicular accelerations much more likely to be linked with large mis-alignments; however, it is noteworthy that some jet features with small perpendicular accelerations do have large mis-alignment angles, perhaps because they experienced acceleration

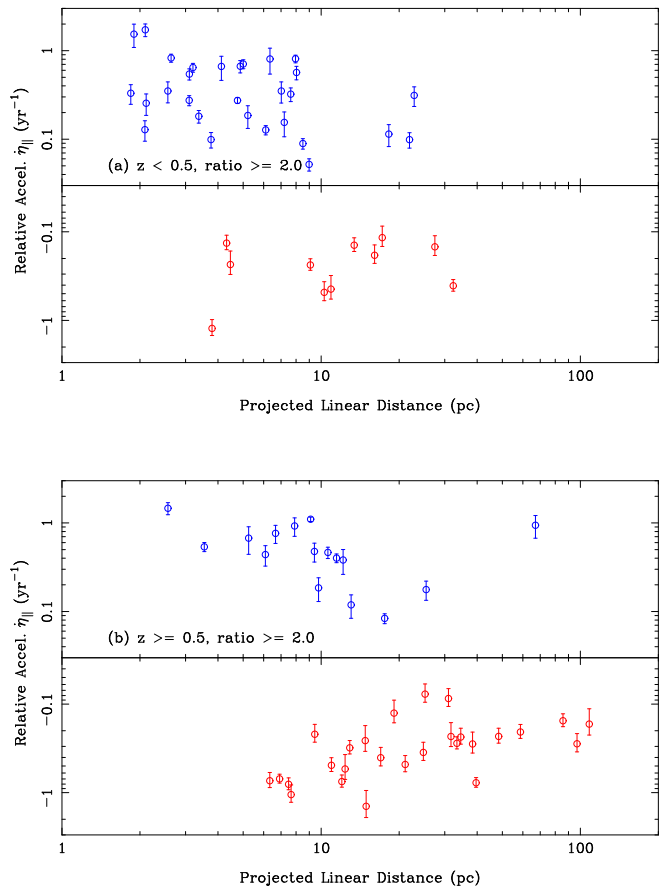


**Figure 5.** Relative parallel accelerations,  $\dot{\eta}_{\parallel}$  for all jet features with  $\geq 3\sigma$  parallel accelerations and with parallel to perpendicular acceleration ratios  $\geq 2.0$ . Accelerations are plotted against average projected linear distance from the core position in parsecs. Sources with redshifts  $z < 0.5$  are plotted in panel (a), and sources with redshifts  $z \geq 0.5$  are plotted in panel (b). In panel (a), five features from NGC 1052 at projected linear distances  $< 1.0$  pc are not plotted for clarity; four of these have positive acceleration, and one has negative.

prior to our monitoring period.

Figure 8 plots relative perpendicular acceleration versus proper motion mis-alignment angle<sup>15</sup> for all jet features with both significant perpendicular acceleration and significant non-radial motion. Positive perpendicular acceleration will tend to increase  $\phi$  over time, so the observed accelerations are overwhelmingly (52 out of 59 features) in the correct direction to have caused the observed mis-aligned motion.

Knowing that observed perpendicular accelerations cause the observed mis-aligned motions does not tell us why the features are changing direction to become non-radial. Kellermann et al. (2004) showed that the non-radial motion of jet features tends to be in the direction of the downstream emission, suggesting that jets follow pre-established channels of flow. This result was confirmed in Paper VII. Here we examine the relationship with *upstream* emission as defined by the mean inner jet position angle. In Paper X, we calculated the mean inner jet position angle by averaging all CLEAN components in the radio map between radii of 0.15 and 1.0 mas from

<sup>15</sup> Note the convention  $\phi - \langle \vartheta \rangle$  is the opposite of that chosen in Figure 10 in Paper VII; however, this sign definition simplifies the discussion.

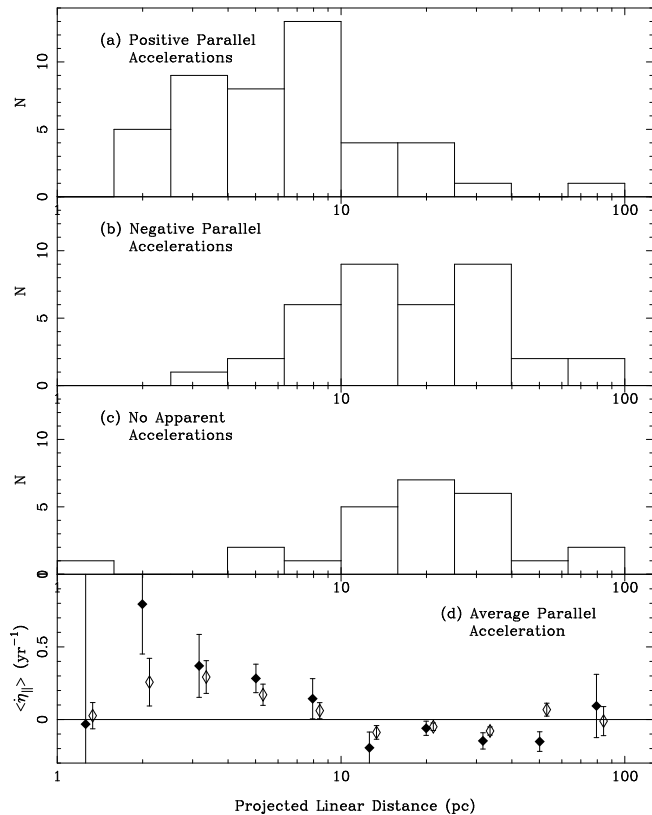


**Figure 6.** Histograms of projected linear distance for jet features with positive parallel accelerations (panel (a)), negative parallel accelerations (panel (b)), and no apparent acceleration (panel (c)). Panels (a) and (b) only include features with parallel accelerations significant at the  $\geq 3\sigma$  level and with parallel to perpendicular acceleration ratios  $\geq 2.0$ . Panel (c) selects features with no significant acceleration and robustly small parallel and perpendicular accelerations defined by  $|\dot{\eta}_{\parallel,\perp}| + 2\sigma \leq 0.1$ . Note that seven features from NGC 1052 at projected linear distances  $< 1.0$  pc are not plotted in the above three panels for clarity; four of these have positive acceleration, one has negative acceleration, and two have no apparent acceleration. In Panel (d), solid diamonds show the unweighted average of the relative parallel accelerations in each projected distance bin for the features plotted in the above panels. Open diamonds give the average acceleration in each projected distance bin using all features in Table 1, regardless of significance level of the acceleration measurement.

the optically thick core feature near the base of the jet. This calculation was performed for all epochs, resulting in a circular mean and standard deviation for the inner jet position angle for each source. We note that, as described in Paper X, mean inner jet position angles were not available for all sources in our sample due to insufficient time coverage or number of epochs, core identification uncertainty, counter-jet emission, or highly curved jet structure within 1 mas of the core. Note that the circular standard deviation in the jet position angle is mainly due to the variability in jet position angle over time as newly emitted jet features emerge at different position angles (Paper X).

In Figure 9 we plot both non-radial motion misalignment angle and relative perpendicular acceleration against the offset between the first epoch structural position angle of a jet feature,  $\vartheta_{first}$ , and the mean of the inner jet position angle, JetPA. Our key question is whether jet features that start out with a large offset between their structural position angle and the mean

inner jet position angle experience kinematics that tend to bring them into better alignment with the inner jet position angle. We define a ‘large offset’ to be a first epoch structural position angle that is more than one standard deviation from the mean inner jet position angle, where the circular standard deviation is computed for the set of inner jet position angles across all epochs in which that source was observed. It is also important that we only consider jet features with mean angular distance  $\langle R \rangle \geq 2.0$  mas to avoid the possibility that the jet feature we are studying contributes significantly to the mean of the inner jet position angle<sup>16</sup>.

Both the observed non-radial motions and perpendicular accelerations have a strong tendency to be in the correct direction to move the jet feature toward the direction of the mean inner jet position angle, indicating some sort of collimating effect prevents features from moving along a ballistic trajectory. The odds of at least 35 out of 46 non-radial motions and 16 out of 21 perpendicular accelerations having this tendency by pure chance are  $P = 0.00027$  and  $P = 0.013$ , respectively.

As a diagnostic of this relationship, Figure 10 plots each of the jet features in Figure 9(a) at their first epoch position with an arrow indicating the direction of their velocity vector. Jet features from different sources are included on the plot by using projected linear distance in parsecs and rotating the position angles to place the mean inner jet position angle of each source along the  $x$ -axis in the figure. The inset of Figure 10 clearly shows that the tendency for jet features to experience motions that move them toward better alignment with the mean inner jet position angle is very strong for features at small projected linear distance. Almost all (16 out of 17) features plotted in the inset have this tendency; however, for jet features first observed at larger distances, the tendency is much weaker (19 out of 29) and more consistent with pure chance. At these larger projected distances, jets may have already experienced bends, and those jet features may be following the bends as indicated in Kellermann et al. (2004) and Paper VII.

#### 4. DISCUSSION

We find that apparent accelerations in the motion of jet features are common, with approximately half of the motions we studied showing significant accelerations parallel and/or perpendicular to their velocity vector. We find at least one significantly accelerating feature in three-quarters of the blazar jets in our sample. Parallel accelerations, indicating changes in apparent speed, are a factor of two times larger on average than perpendicular accelerations associated with changes in direction. This confirms our result from Paper VII, also verified by Piner et al. (2012), that parallel accelerations cannot be the result of jet bending alone.

As demonstrated in Paper VII and summarized in §2, changes in jet direction can change the apparent speed of jet features; however, due to projection effects, we expect to see even larger changes in velocity direction on the sky (i.e. perpendicular accelerations). From the beaming characteristics of a typical parsec-scale flux-density lim-

<sup>16</sup> Including those features with  $\langle R \rangle < 2.0$  mas, strengthens the statistical relationships we find, but this may be an artifact of those features moving toward their own mean position.

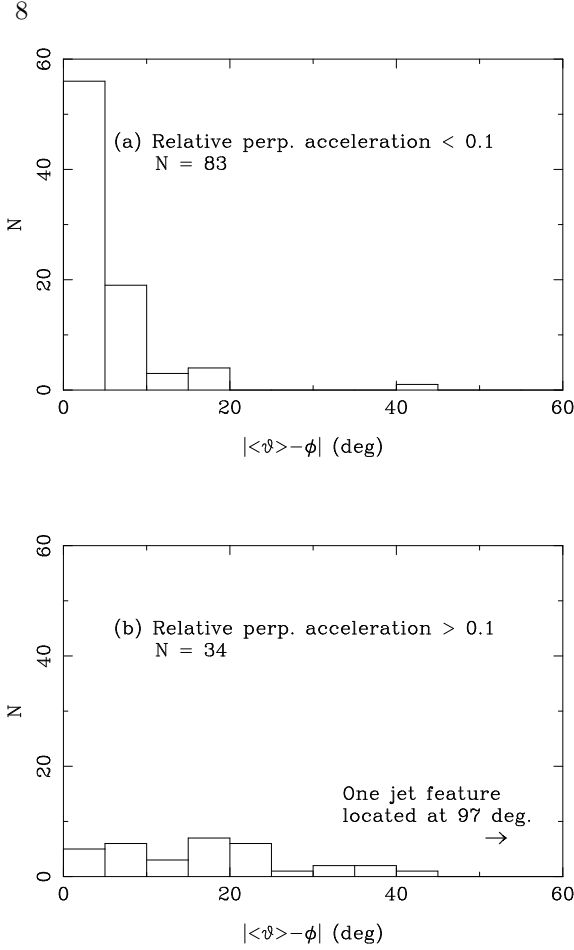


**Figure 7.** Histograms of the magnitude of the misalignment angle,  $|\langle \vartheta \rangle - \phi|$ , for jet features with small perpendicular accelerations (panel (a)) of  $|\dot{\eta}_{\perp}| + 2\sigma < 0.1$  and those with large perpendicular acceleration (panel (b)) of  $|\dot{\eta}_{\perp}| - 2\sigma > 0.1$ .

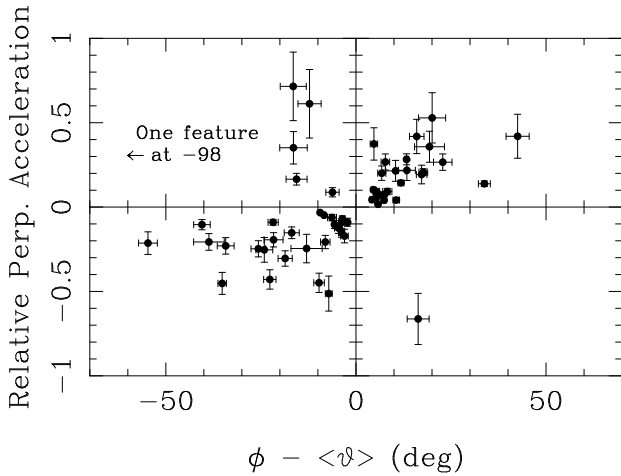


**Figure 8.** Plot of relative perpendicular acceleration,  $\dot{\eta}_{\perp}$ , vs. non-radial motion misalignment angle for jet features with  $\geq 3\sigma$  significant perpendicular acceleration and non-radial motion. Of the 59 features plotted, 52 have acceleration in the correct direction to have caused the observed misalignment (i.e., are located in the 1st and 3rd quadrants).

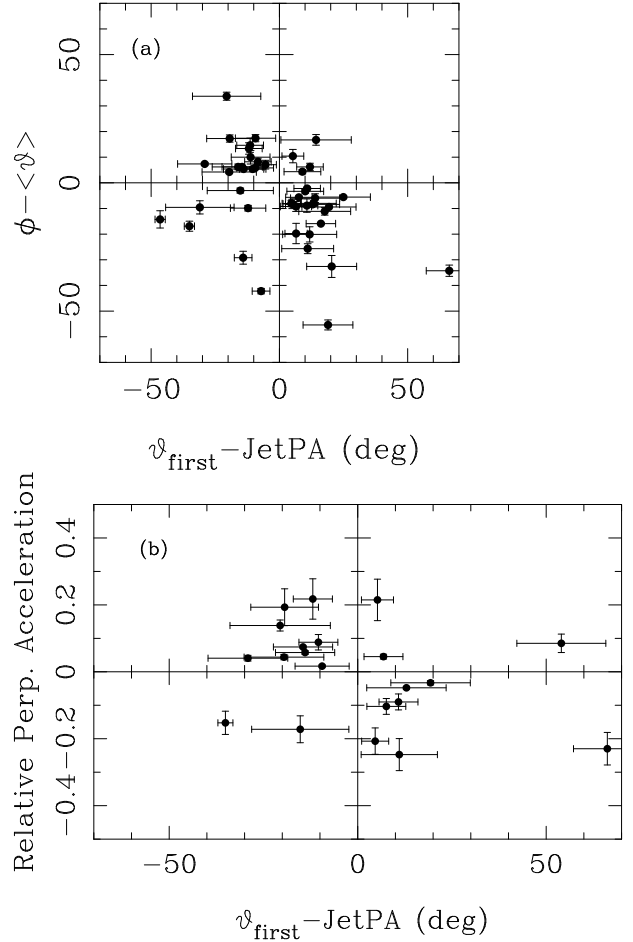


**Figure 9.** Plots of non-radial motion misalignment angle,  $\phi - \langle \vartheta \rangle$ , and relative perpendicular acceleration,  $\dot{\eta}_{\perp}$ , versus initial structural angle misalignment,  $\vartheta_{\text{first}} - \text{JetPA}$  for jet features at  $\langle R \rangle \geq 2.0$  mas with  $\geq 3\sigma$  non-radial motion (panel (a)) or perpendicular accelerations (panel (b)). Here  $\vartheta_{\text{first}}$  is the structural position angle of the feature in the first epoch it was observed, and JetPA is the mean position angle of the inner jet over all epochs as defined in Paper X. Note that the  $x$ -axis error bars indicate the standard deviation of inner jet position angle over in all epochs that source was observed. Only jet features with an initial structural position angle outside the standard deviation of inner jet position angle measurements are plotted. In general, the observed non-radial motions and perpendicular accelerations are in the correct direction to move the jet feature toward the mean position angle of the inner jet (35 of the 46 plotted non-radial motions, 16 of the 21 of the plotted perpendicular accelerations).

ited sample, Paper VII showed that parallel accelerations due to bending alone should be only 60% of the magnitude of the accompanying perpendicular accelerations. Here we see almost the opposite ratio, with parallel accelerations nearly a factor of two times the magnitude of perpendicular accelerations. While for any given jet feature, we cannot confidently ascribe an apparent parallel acceleration to a change in Lorentz factor; we conclude that, on average, changes in the Lorentz factors of jet features dominate the observed parallel accelerations.

#### 4.1. Lorentz Factor vs. Jet Distance

Paper VII reported an overall tendency for jet features with positive parallel acceleration to be at smaller projected linear distances than jet features with negative parallel acceleration, with a fuzzy break between positive and negative acceleration occurring at  $\sim 15$  pc.



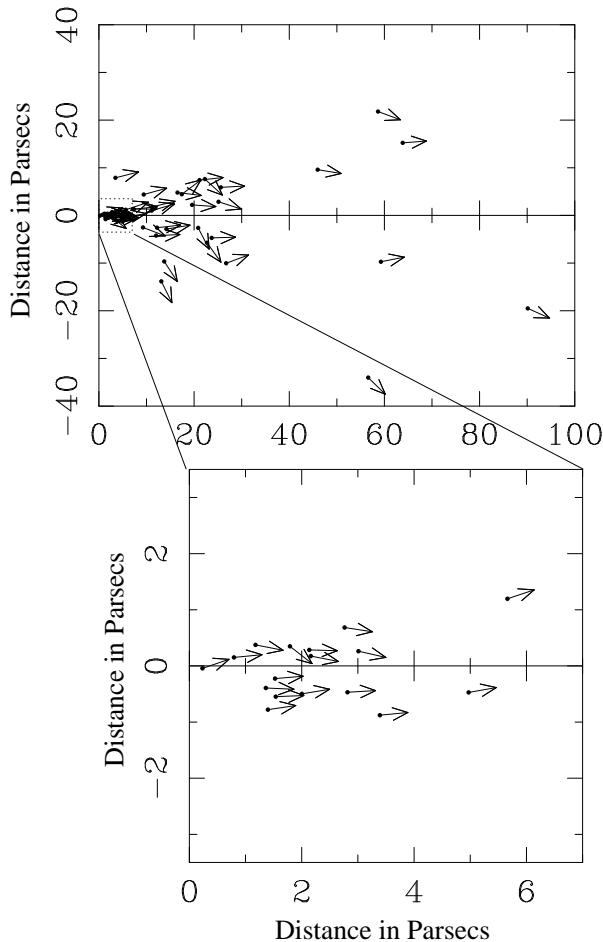


**Figure 10.** Locations of the 46 jet features plotted in Figure 9(a) in their first epoch of observation with an arrow showing the direction of their mean velocity vector. Positions of jet features from multiple sources are plotted together with projected linear distance from the core, given in parsecs. The locations of the features for each source are rotated so that the  $x$ -axis represents the mean inner jet position angle. The inset shows the details of the cluster of features at short projected distances.

Piner et al. (2012) confirmed the tendency for a dominance of positive accelerations at short projected distances  $< 15$  pc, but their smaller sample, focused on compact sources, did not allow them to measure the acceleration of more than a few features beyond this distance. In an earlier, smaller study of  $\gamma$ -ray blazars at 43 GHz, Jorstad et al. (2005) reported accelerations in nine of the fifteen jets they studied, and these tended to be positive parallel accelerations near the base of jet, although they could not determine whether the observed accelerations were due to changes in intrinsic speed or direction of the jet features.

Figures 3 through 6 explore this relationship and we clearly confirm the tendency for jet features with positive parallel acceleration (speeding up) to appear at shorter projected linear distances than jet features with negative parallel acceleration (slowing down), with much better statistics than we achieved in Paper VII. It is noteworthy that Figure 3(b) shows no relationship if the accelerations are plotted against *angular* distance, the direct observable in our maps and motion fitting, thus ruling out simple observational biases. Projected *linear* distance depends on source redshift, so we also investigated this

relationship in both low and high redshift groups (Figure 5) and found it holds in both separately.

Figure 4 tests this relationship as a function of parallel/perpendicular acceleration ratio. As discussed above, accelerations of jet features with high parallel/perpendicular ratios are expected to be more likely to be due to changes in Lorentz factor. If this is true *and* if the relationship with jet distance is due to changes in Lorentz factor, we would expect the relationship with jet distance to be stronger for jet features with a high parallel/perpendicular ratio, and that is precisely what we found.

Finally, Figure 6 compares these high parallel/perpendicular ratio accelerating features to each other and to a set of features that we can be confident have little, if any, apparent acceleration. Jet features with positive parallel acceleration are clearly at smaller projected distance than negatively accelerating features or features with no apparent acceleration; however, features with negative apparent acceleration do not appear to differ in their distance distribution from jet features with no apparent acceleration. The final panel of Figure 6 shows the average acceleration in each distance bin and clearly indicates a decrease from strong positive acceleration at short distances to slightly negative acceleration at distances  $\gtrsim 10$  pc.

Equation 4 allows us to estimate the relative change in Lorentz factor in the galaxy frame under the assumption that all of the observed relative acceleration is due to Lorentz factor changes. If  $\Gamma$  is sufficiently greater than unity, then  $\beta \simeq 1$  and  $\dot{\Gamma}/\Gamma \simeq \dot{\eta}_{\parallel}/\delta^2$ . The average positive relative accelerations range from 0.1 to 1.0  $\text{yr}^{-1}$  for projected distances  $\lesssim 10$  pc in Figure 6(d). Assuming Doppler factors of order  $\delta \sim 10$ , the implied positive acceleration in the core region falls in the range  $\dot{\Gamma}/\Gamma \simeq 10^{-3}$  to  $10^{-2}$  per year in the galaxy frame. Due to our detection of several rapidly accelerating features at small projected distances, the rates of change estimated above are up to an order of magnitude larger than those estimated in Paper VII and found by Piner et al. (2012) in their sample.

It is important to note that while rates of intrinsic change in range  $\dot{\Gamma}/\Gamma \simeq 10^{-3}$  to  $10^{-2}$  per year may seem modest, they are acting over very long periods of time in the frame of the AGN host galaxy where a decade of observed time in our frame may span centuries. A jet feature at a projected distance of 10 pc actually lies  $\sim 10^2$  pc from the nucleus, assuming a typical order of magnitude de-projection factor in a highly beamed jet. This large de-projected distance indicates that the process of acceleration of features in the jet flow may span hundreds of light years in the source frame. As we show in §4.1.1, the observed accelerations are in many cases sufficient to double or triple the apparent speed of a moving feature during our observations, suggesting a corresponding change in the Lorentz factor of the same order.

Beyond projected distances of  $\sim 10$  pc, jet features are more likely to show negative acceleration or no detectable acceleration with average observed accelerations in the range 0.0 to  $-0.2 \text{ yr}^{-1}$  corresponding to source frame Lorentz factor decreases in the range  $\dot{\Gamma}/\Gamma \sim -10^{-3}$  per year. As discussed in Paper VII, Lorentz factor decreases of this magnitude would completely decelerate jets before

they reach scales of tens to hundreds of kiloparsecs; however, Lorentz factor decreases brought about by interaction with the inter-stellar medium would be expected to decrease in magnitude with distance from the center of the galaxy.

#### 4.1.1. Apparent Speed vs. Distance

Measurements of apparent speeds of different jet features in the same source have been used as evidence that jets show positive acceleration on parsec scales, with features at small projected distances appearing to be slower than features found further away (Krichbaum et al. 1998; Cotton et al. 1999; Homan et al. 2001; Piner et al. 2007; Britzen et al. 2008a; Piner et al. 2012). Paper X reported a general trend of increasing apparent speed with distance down the jet for radio galaxies and BL Lac objects. Plots of apparent speed versus distance in M87 by Meyer et al. (2013) and Asada et al. (2014) show increasing apparent speed out to projected linear distances of  $\sim 70$  pc at HST-1 and decreasing apparent speed at larger distances. Note that the de-projection factor for M87 is only a factor of 2 – 4 assuming a viewing angle in the range  $15 - 25^\circ$  (Acciari et al. 2009), so the de-projected transition from increasing speed to constant or decreasing speed occurs at  $\sim 10^2$  pc, consistent with our estimates in the previous section.

In this section we discuss plots of apparent speed versus projected linear distance which include *speed profiles* for our accelerating jet features. A speed profile is simply a plot of our best fit accelerating kinematic model to show the apparent speed of the feature as a function of projected linear distance down the jet. We show these speed profiles only for the inner 60% of our observed time range to avoid inadequate extrapolation of the instantaneous speeds deduced from our kinematic models beyond the point where they are well supported by the data.

Figure 11 shows individual source plots for all 33 jets which have at least four jet features suitable for acceleration analysis in this paper. Speed profiles are only plotted for features showing significant parallel and/or perpendicular acceleration. Other jet features studied in this paper without significant acceleration are plotted as solid squares, and we’ve included all the remaining robust jet features from Paper X as open circles. Clear increases in apparent speed with projected linear distances are seen in many of the jets, e.g., 1928+738. A trend of decreasing speeds at larger distances is seen in several cases as well. These trends are noisy but generally support our conclusions from the acceleration measurements themselves in the previous section.

As discussed in Paper X, jet features in an individual source can have a large dispersion in apparent speeds. Figure 11 shows that this dispersion is partly due to the observed acceleration and deceleration along the jet with distance; however, even at a fixed distance, there can be a large dispersion in apparent speeds in a given source, e.g. 1226+023 (3C 273). As shown in Paper X, viewing angle differences between features in the same jet are expected to cause some dispersion in apparent speed; however, we argue there that the conditions necessary to produce a large dispersion due to viewing angle alone should also cause the jets to have a wide opening angle on the sky. The same conditions should also produce large perpendicular accelerations when jet features change their tra-

jectory, and we already conclude above that jet features primarily change their apparent speed due to changes in their Lorentz factor, not due to changes in their viewing angle. Hence we conclude that even at a fixed projected distance in an individual source, jet features can show a range of apparent speed due, at least in part, to differences in their Lorentz factors.

Finally, we consider the speed profile plot for our sample as a whole. Figure 12(a) collects the speed profiles for all jet features showing significant parallel and/or perpendicular accelerations. Those accelerations that are most likely to be caused by changes in Lorentz factor, as indicated by a parallel/perpendicular acceleration ratio  $\geq 2.0$ , are plotted in either blue or red for positive and negative accelerations, respectively. Panel (b) includes all the other features studied in this paper without significant acceleration as solid squares and the remaining robust features from Paper X as open circles. The apparent speed distribution has the largest values in the range  $40 - 50c$  at a projected linear distance of  $\sim 10$  pc.

#### 4.1.2. Lorentz Factors, Shocks, and The Jet Flow

The Lorentz factors described above are for the moving jet features, and they may not represent the Lorentz factor of the flow directly. Propagating shocks, proposed to explain both variability and VLBI jet features, are expected to travel at a different speed from flow (e.g. Hughes et al. 1985; Marscher & Gear 1985), and fast forward moving shocks can appear to move at two to three times the speed of the flow (Cohen et al. 2014; Aller et al. 2014). Agudo et al. (2001) show that a piston driven shock, where there is an injection of new material into the flow with a higher than usual Lorentz factor, will produce a leading moving feature that is nearly at the speed of the higher Lorentz factor; however, it will also generate a number of slower, trailing shocks which appear to accelerate with the underlying background flow. The picture is further complicated if one considers three dimensional effects of ejections of new moving features at multiple position angles (Aloy et al. 2003). Therefore a range of shock strengths and types, along with changes in the injection speed or direction of new material, could plausibly account for the dispersion we see in jet feature speeds at a given distance in a jet.

A traveling shock can change its speed if the underlying conditions in the jet change, it dissipates its energy, or it interacts with other propagating disturbances in the flow. To produce the broad trends we see for accelerating features increasing their speed at small distances and decreasing their speed at large distances, a wide range of shock types and strengths across many features and sources would need to change their speed in a similar fashion over time and distance in the jet. Given that shock speeds in the flow are added relativistically to the flow speed to determine the apparent speed of a moving feature, a natural common thread for a diversity of shock types and strengths is the flow speed itself, as illustrated by the trailing shocks in the numerical simulation of Agudo et al. (2001). We suggest that the acceleration of the flow itself is responsible for the broad trends we observe, and that the jet flow acceleration region extends out to de-projected distances of order  $10^2$  pc, beyond which the flow begins to decelerate or remains constant.

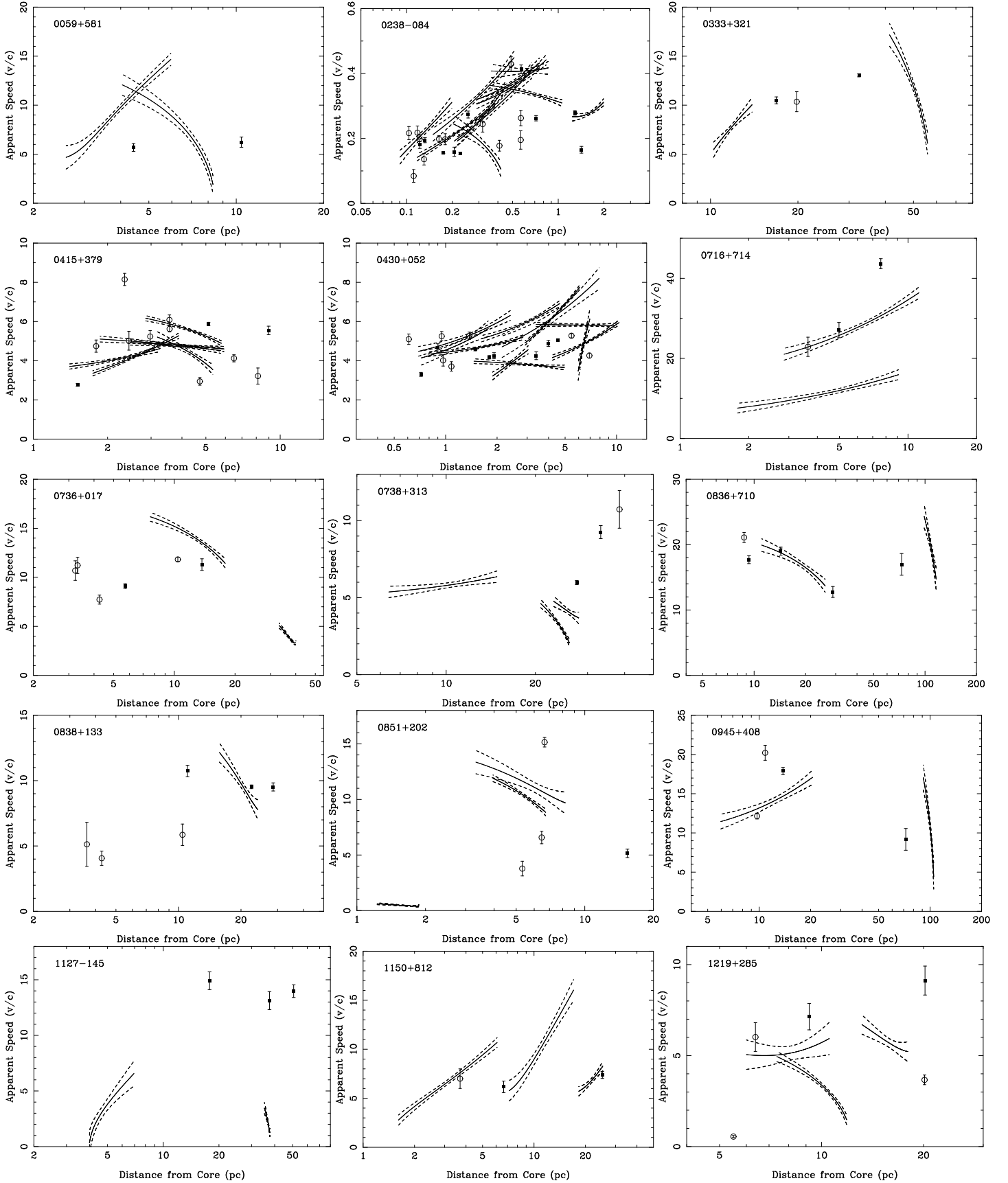


**Figure 11.** Plots of apparent speed vs. projected linear distance for all sources with four or more jet features in Table 1. Features with significant acceleration are plotted as linear projections of their fitted motion with one-sigma uncertainties defined by the upper and lower dashed lines. Features without significant accelerations are plotted as solid squares at the projected location of the midpoint of their motion. The apparent proper motion of other robust features from Paper X are plotted as open circles.

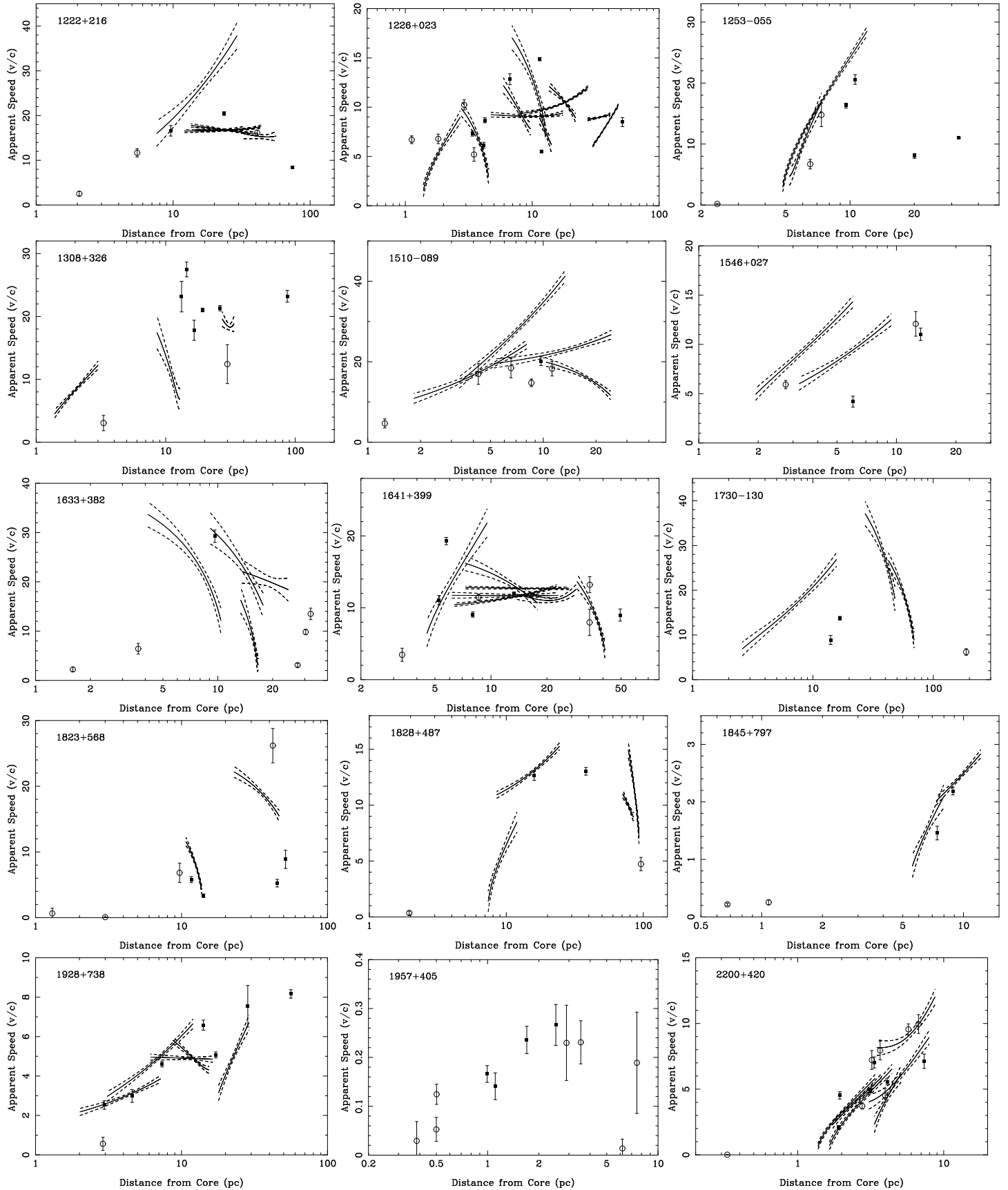


Figure 11. Figure continued from previous page.

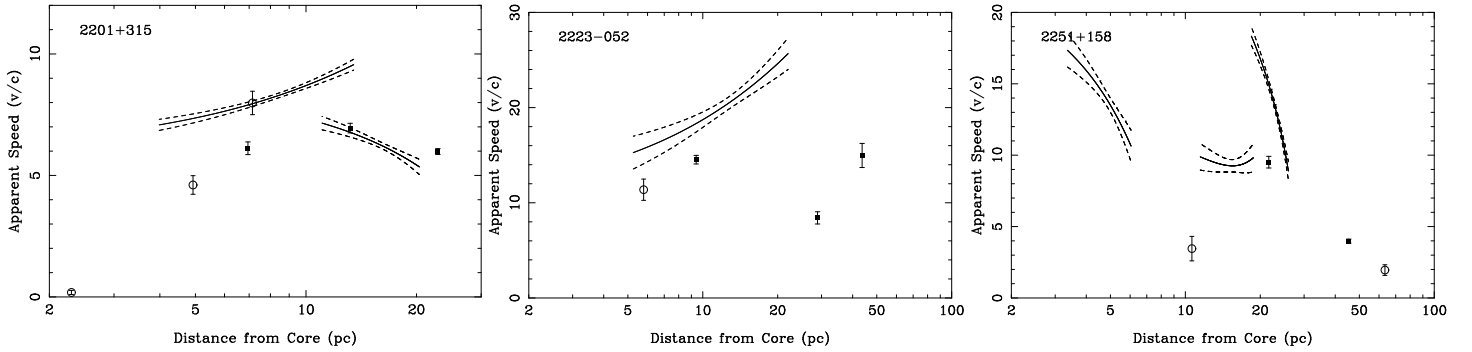
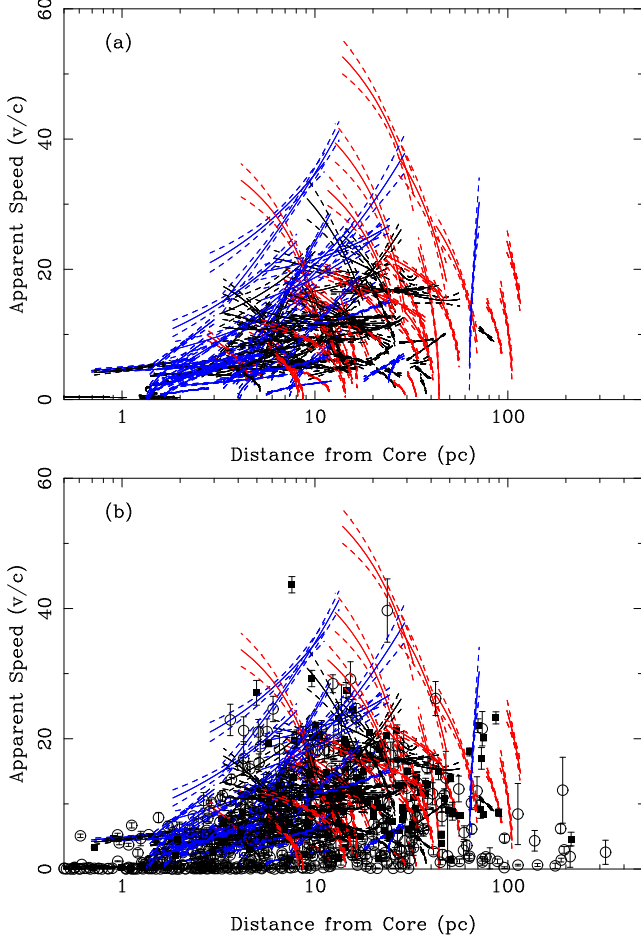


Figure 11. Figure continued from previous page.



**Figure 12.** Plots of apparent speed vs. projected linear distance for all sources with known redshifts. In panel (a), 159 features with significant acceleration are plotted as linear projections of their fitted motion with one-sigma uncertainties defined by the upper and lower dashed lines. Features plotted as blue and red trajectories have parallel/perpendicular acceleration ratios  $\geq 2.0$ , indicating they are more likely to be due to real changes in Lorentz factor. The colors, blue and red, indicate positive and negative parallel acceleration respectively for these 88 features, and the rest are plotted in black. For clarity, six features in NGC 1052 with projected linear distances  $< 0.5$  pc are not plotted in panel (a). Panel (b) adds points representing the motion of 653 features for all sources with known redshifts in our sample. Features studied in this paper without significant accelerations are plotted as solid squares at the projected location of the midpoint of their motion. The apparent proper motion of the other robust features from Paper X are plotted as open circles. A total of 40 features with projected linear distances  $< 0.5$  pc and small motions are not plotted in panel (b).

#### 4.2. Non-radial Motions and Jet Collimation

Non-radial motions, or motions that do not extrapolate back to the jet origin, comprise approximately half of our sample, indicating that jet features often do not follow ballistic trajectories. Observed perpendicular accelerations are almost always in the correct direction to have caused the non-radial motion in that feature; however, we note that some jet features have non-radial motions without significant perpendicular acceleration. These features without detectable perpendicular acceleration, or the few with perpendicular acceleration in the wrong direction, may have experienced earlier periods of bending that changed their direction of motion prior to our observations.

Earlier work has shown that non-radial jet features typically have their direction of motion rotated to better align with downstream emission (Kellermann et al. 2004, and Paper VII), indicating that the jet is following pre-established channels and jet features move around the bends (Kellermann et al. 2004). In §3.2 we investigate the relationship between non-radial motion and *upstream* emission, specifically the mean inner jet position angle. We find that jet features that start out with a structural position offset from the mean inner jet direction tend to experience kinematics which will bring them into better alignment. This tendency of the motions to better align with the mean inner jet direction is strongest for jet features at small projected distances,  $\lesssim 10$  pc from the core region, suggesting that active collimation of the flow continues out to similar distances as the acceleration discussed in the previous section, i.e.  $\sim 10^2$  parsecs de-projected. A connection between acceleration and collimation of the flow is expected in magnetic acceleration models which can continue to operate at large distances from the jet origin (e.g. Vlahakis & Königl 2004; Komissarov et al. 2007; Lyubarsky 2009). Helical magnetic fields required by these models are suggested by a growing body of observational evidence from Faraday rotation (e.g. Asada et al. 2002; Gabuzda et al. 2004; Asada et al. 2010; Hovatta et al. 2012; Zamaninasab et al. 2013; Gabuzda et al. 2014).

In a pure conically expanding flow, jet features would be free to move ballistically, so our result suggests that the jet width,  $W_j$ , is expanding less rapidly than  $W_j \propto r$ , unless jet features at large initial position angles have helical streaming motions that only make them appear to return toward the jet axis (e.g. Hardee et al. 2005). Only partial helical trajectories for individual features have been observed to date (e.g. Savolainen et al. 2006b;

Molina et al. 2014), and the wavelength of any such motion would have to be tuned to match the length scales observed here. Collimation of the jet itself is consistent with structural studies of M87 which show an edge-brightened jet (Junor et al. 1999; Kovalev et al. 2007) with an opening angle that narrows with distance from the core (Junor et al. 1999). Asada & Nakamura (2012) and Hada et al. (2013) find  $W_j \propto r^{0.6}$  for M87, and Nagai et al. (2014) find a more rapid collimation profile in 3C 84 of  $W_j \propto r^{0.25}$ . We note that Asada & Nakamura (2012) report that the jet of M87 maintains parabolic streamlines out to the location of HST-1 at a de-projected location of  $\sim 10^2$  parsecs where the maximum apparent speeds are observed, as discussed above.

## 5. SUMMARY AND CONCLUSIONS

We have analyzed acceleration and other kinematic data for 329 jet features in 95 sources. Our main findings are as follows:

(i) Accelerations and non-ballistic trajectories are common in the motions of jet features. Significant parallel accelerations, indicating a change in speed, occur in 37% of the jet features in our sample, and nearly a quarter (23%) have significant perpendicular accelerations indicating a change in direction. Nearly half (47%) of our sample show significant non-radial motion that does not extrapolate back to the jet origin.

(ii) In general parallel accelerations are distinctly larger than perpendicular accelerations. The typical magnitudes of parallel accelerations are nearly a factor of two times the perpendicular accelerations, indicating that, on average, changes to the Lorentz factors of jet features dominate the observed parallel accelerations.

(iii) Parallel accelerations tend to be positive near the jet base, at short projected distance, and negative at longer distances. The transition between speeding up and slowing down seems to occur at roughly  $\sim 10 - 20$  pc projected distance, with significant scatter. Plots of apparent speed versus distance confirm this broad relationship both for the entire sample and in individual sources, but again with significant scatter. It is not uncommon for the range of apparent speeds at a fixed distance in an individual jet to span a factor of two to three, indicating that a diversity of shock strengths and types may play a role in determining the apparent motions of different features in the same jet. We argue that while different types of shocks may explain the diversity of speeds at a given distance, they cannot easily explain the overall trends of individual features speeding up and slowing down across time and distance in the jet. We suggest that the common thread that produces this trend is an overall acceleration of the jet flow out to de-projected distances of order  $10^2$  parsecs, beyond which the flow begins to decelerate or remains constant in speed.

(iv) For a typical Doppler beaming factor of  $\delta \sim 10$ , we estimate the implied Lorentz factor changes of accelerating jet features fall in the range  $\dot{\Gamma}/\Gamma \simeq 10^{-3} - 10^{-2}$  per year in the host galaxy rest frame. While rates of change of this order may appear small, they act over very long periods of time. A typical decade-long observation may correspond to centuries in the host galaxy due to the extreme time compression created by motion near our line of sight. As our plotted speed profiles show, these intrinsic rates of change are sufficient to change apparent

speeds by factors of two to three in many cases, indicating total Lorentz factor changes of a similar magnitude.

(v) The non-radial motion and perpendicular accelerations of jet features that start out with large offsets from the mean inner jet direction are typically in the correct direction to better align those features with the inner jet direction. This connection between directional changes and upstream emission is strongest for jet features at small linear distances,  $\lesssim 10$  pc projected, indicating the jet is still becoming collimated on length scales similar to the observed acceleration. However, we note that motion along helical stream lines for individual jet features could reproduce this result while still allowing the jet envelope to expand conically, although conical expansion was not observed in structural studies of the nearby jets M87 or 3C 84 (e.g. Asada & Nakamura 2012; Nagai et al. 2014).

Special thanks to the other members of the MOJAVE team for contributions to this project. The MOJAVE project was supported under NASA-*Fermi* grants NNX08AV67G and NNX12A087G. DCH was supported by NSF grant AST-0707693. YYK was supported by the Russian Foundation for Basic Research (project 13-02-12103), Research Program OFN-17 of the Division of Physics, Russian Academy of Sciences, and the Dynasty Foundation. ABP was supported by the ‘‘Non-stationary processes in the Universe’’ Program of the Presidium of the Russian Academy of Sciences. TS was partly supported by the Academy of Finland project 274477. ER was partially supported by the Spanish MINECO projects AYA2009-13036-C02-02 and AYA2012-38491-C02-01 and by the Generalitat Valenciana project PROMETEO/2009/104, as well as by the COST MP0905 action ‘Black Holes in a Violent Universe’. This work made use of the Swinburne University of Technology software correlator (Deller et al. 2011), developed as part of the Australian Major National Research Facilities Programme and operated under licence. This research has made use of NASA’s Astrophysics Data System.

## REFERENCES

- Acciari, V. A., Aliu, E., Arlen, T., et al. 2009, *Science*, 325, 444
- Agudo, I., Gómez, J.-L., Martí, J.-M., et al. 2001, *ApJ*, 549, L183
- Aller, M. F., Hughes, P. A., Aller, H. D., Latimer, G. E., & Hovatta, T. 2014, *ApJ*, 791, 53
- Aloy, M.-Á., Martí, J.-M., Gómez, J.-L., et al. 2003, *ApJ*, 585, L109
- Asada, K., Inoue, M., Uchida, Y., Kameno, S., Fujisawa, K., Iguchi, S., & Mutoh, M. 2002, *PASJ*, 54, L39
- Asada, K., & Nakamura, M. 2012, *ApJ*, 745, L28
- Asada, K., Nakamura, M., Doi, A., Nagai, H., & Inoue, M. 2014, *ApJ*, 781, L2
- Asada, K., Nakamura, M., Inoue, M., Kameno, S., & Nagai, H. 2010, *ApJ*, 720, 41
- Britzen, S., et al. 2008, *A&A*, 484, 119
- Cohen, M. H., Meier, D. L., Arshakian, T. G., et al. 2014, *ApJ*, 787, 151
- Cotton, W. D., Feretti, L., Giovannini, G., Lara, L., & Venturi, T. 1999, *ApJ*, 519, 108
- Danforth, C. W., Nalewajko, K., France, K., & Keeney, B. A. 2013, *ApJ*, 764, 57
- Deller, A. T., Brisken, W. F., Phillips, C. J., et al. 2011, *PASP*, 123, 275
- Gabuzda, D. C., Cantwell, T. M., & Cawthorne, T. V. 2014, *MNRAS*, 438, L1
- Gabuzda, D. C., Murray, É., & Cronin, P. 2004, *MNRAS*, 351, L89
- Gómez, J.-L., Marscher, A. P., Alberdi, A., Jorstad, S. G., & Agudo, I. 2001, *ApJ*, 561, L161
- Hada, K., Kino, M., Doi, A., et al. 2013, *ApJ*, 775, 70
- Hardee, P. E., Walker, R. C., & Gómez, J. L. 2005, *ApJ*, 620, 646
- Hinshaw, G., Weiland, J. L., Hill, R. S., et al. 2009, *ApJS*, 180, 225
- Homan, D. C., Kadler, M., Kellermann, K. I., et al. 2009, *ApJ*, 706, 1253
- Homan, D. C., Lister, M. L., Kellermann, K. I., Cohen, M. H., Ros, E., Zensus, J. A., Kadler, M., & Vermeulen, R. C. 2003, *ApJ*, 589, L9
- Homan, D. C., Ojha, R., Wardle, J. F. C., Roberts, D. H., Aller, M. F., Aller, H. D., & Hughes, P. A. 2001, *ApJ*, 549, 840
- Hovatta, T., Lister, M. L., Aller, M. F., et al. 2012, *AJ*, 144, 105
- Hughes, P. A., Aller, H. D., & Aller, M. F. 1985, *ApJ*, 298, 301
- Jorstad, S. G., Marscher, A. P., Lister, M. L., Stirling, A. M., Cawthorne, T. V., Gómez, J.-L., & Gear, W. K. 2004, *AJ*, 127, 3115
- Jorstad, S. G., et al. 2005, *AJ*, 130, 1418
- Junor, W., Biretta, J. A., & Livio, M. 1999, *Nature*, 401, 891
- Kellermann, K. I., Vermeulen, R. C., Zensus, J. A., & Cohen, M. H. 1998, *AJ*, 115, 1295
- Kellermann et al., 2004, *ApJ*, 609, 539
- Kovalev, Y. Y., et al. 2005, *AJ*, 130, 2473
- Kovalev, Y. Y., Lister, M. L., Homan, D. C., & Kellermann, K. I. 2007, *ApJ*, 668, L27
- Komissarov, S. S., Barkov, M. V., Vlahakis, N., & Königl, A. 2007, *MNRAS*, 380, 51
- Komissarov, S. S. 2011, *Mem. Soc. Astron. Italiana*, 82, 95
- Krichbaum, T. P., Alef, W., Witzel, A., et al. 1998, *A&A*, 329, 873
- Lister, M. L., et al., 2009, *AJ*, 137, 3718
- Lister, M. L., Aller, M. F., Aller, H. D., et al. 2013, *AJ*, 146, 120
- Lister, M. L., Cohen, M. H., Homan, D. C., et al. 2009, *AJ*, 138, 1874
- Lister, M. L., & Homan, D. C. 2005, *AJ*, 130, 1389
- Lister, M. L. & Marscher, A. P. 1997, *ApJ*, 476, 572
- Lyubarsky, Y. 2009, *ApJ*, 698, 1570
- Marscher, A. P., & Gear, W. K. 1985, *ApJ*, 298, 114
- Meier, D. L., Koide, S., & Uchida, Y. 2001, *Science*, 291, 84
- Meyer, E. T., Sparks, W. B., Biretta, J. A., et al. 2013, *ApJ*, 774, L21
- Molina, S. N., Agudo, I., Gómez, J. L., et al. 2014, *A&A*, 566, A26
- Nagai, H., Haga, T., Giovannini, G., et al. 2014, *ApJ*, 785, 53
- Nilsson, K., Pursimo, T., Sillanpää, A., Takalo, L. O., & Lindfors, E. 2008, *A&A*, 487, L29
- Petrov, L., Gordon, D., Gipson, J., et al. 2009, *Journal of Geodesy*, 83, 859
- Piner, B. G., Mahmud, M., Fey, A. L., & Gospodinova, K. 2007, *AJ*, 133, 2357
- Piner, B. G., Pushkarev, A. B., Kovalev, Y. Y., et al. 2012, *ApJ*, 758, 84
- Savolainen, T., Wiik, K., Valtaoja, E., & Tornikoski, M. 2006, *A&A*, 446, 71
- Savolainen, T., Wiik, K., Valtaoja, E., et al. 2006, *ApJ*, 647, 172
- Sikora, M., Begelman, M. C., Madejski, G. M., & Lasota, J.-P. 2005, *ApJ*, 625, 72
- Vlahakis, N., Königl, A. 2004, *ApJ*, 605, 656
- Wardle, J. F. C., Cawthorne, T. V., Roberts, D. H., & Brown, L. F. 1994, *ApJ*, 437, 122
- Zamaninasab, M., Savolainen, T., Clausen-Brown, E., et al. 2013, *MNRAS*, 436, 3341
- Zensus, J. A., Ros, E., Kellermann, K. I., et al. 2002, *AJ*, 124, 662
- Zensus, J. A., Cohen, M. H., & Unwin, S. C. 1995, *ApJ*, 443, 35

**Table 1**  
Jet Features for Acceleration and Non-Radial Motion Analysis

Source	I.D.	N	$\langle R \rangle$ (mas)	$\langle \theta \rangle$ (deg.)	$d_{proj}$ (pc)	$\mu$ ( $\mu\text{as yr}^{-1}$ )	$\beta_{obs}$	$\phi$ (deg.)	$ \langle \theta \rangle - \phi $ (deg.)	$\dot{\mu}_{  }$ ( $\mu\text{as yr}^{-2}$ )	$\dot{\mu}_{\perp}$ ( $\mu\text{as yr}^{-2}$ )	$\dot{\eta}_{  }$ ( $\text{yr}^{-1}$ )	$\dot{\eta}_{\perp}$ ( $\text{yr}^{-1}$ )
(1)	(2)	(3)	(4)	(5)	(6)	(7)	(8)	(9)	(10)	(11)	(12)	(13)	(14)
0003-066	4	23	6.63	-74.6	32.34	80 ± 6	1.7 ± 0.1	-90.3 ± 2.8	15.6 ± 2.8	-24 ± 3	10 ± 2	-0.41 ± 0.06	0.17 ± 0.03
0010+405	1	10	8.18	-31.3	32.26	428 ± 40	6.9 ± 0.6	-19.2 ± 4.1	12.1 ± 4.1	-43 ± 69	11 ± 53	-0.13 ± 0.20	0.03 ± 0.16
0016+731	1	15	1.19	140.3	10.15	106 ± 4	8.2 ± 0.3	163.2 ± 2.2	22.8 ± 2.4	9 ± 2	10 ± 2	0.23 ± 0.05	0.27 ± 0.05
0059+581	2	21	1.70	-116.3	11.69	168 ± 14	6.2 ± 0.5	-102.0 ± 3.3	14.3 ± 3.5	-16 ± 8	8 ± 5	-0.16 ± 0.08	0.08 ± 0.05
	3	14	0.92	-124.7	6.34	185 ± 13	6.8 ± 0.5	-114.9 ± 3.2	9.8 ± 3.4	-83 ± 15	-16 ± 12	-0.73 ± 0.14	-0.14 ± 0.11
	4	14	0.67	-157.4	4.61	154 ± 11	5.7 ± 0.4	-125.1 ± 4.0	32.3 ± 4.2	-2 ± 14	12 ± 14	-0.02 ± 0.15	0.13 ± 0.15
	5	13	0.53	-163.4	3.65	239 ± 8	8.9 ± 0.3	-120.8 ± 2.9	42.5 ± 3.0	103 ± 13	61 ± 19	0.71 ± 0.09	0.42 ± 0.13
0202+149	5	11	3.11	-66.2	16.72	568 ± 53	14.0 ± 1.3	-56.8 ± 4.3	9.4 ± 4.6	-44 ± 45	21 ± 36	-0.11 ± 0.11	0.05 ± 0.09
	8	11	1.86	-39.3	10.00	358 ± 23	8.8 ± 0.6	-53.1 ± 3.5	13.8 ± 3.9	44 ± 17	-17 ± 17	0.17 ± 0.07	-0.07 ± 0.07
0212+735	1	19	0.89	112.2	7.41	72 ± 2	6.6 ± 0.2	93.5 ± 1.7	18.6 ± 1.9	-6 ± 1	-7 ± 1	-0.27 ± 0.04	-0.30 ± 0.05
0215+015	2	16	2.47	106.3	21.09	344 ± 18	26.1 ± 1.4	100.7 ± 1.6	5.6 ± 1.8	-61 ± 12	-15 ± 7	-0.48 ± 0.10	-0.12 ± 0.05
0224+671	1	13	9.21	-6.0	57.41	267 ± 12	8.3 ± 0.4	-6.7 ± 2.1	0.7 ± 2.1	14 ± 10	15 ± 8	0.08 ± 0.05	0.09 ± 0.04
	4	13	0.52	5.1	3.24	96 ± 12	3.0 ± 0.4	-2.0 ± 1.7	7.1 ± 1.9	21 ± 9	-5 ± 2	0.34 ± 0.15	-0.08 ± 0.03
0234+285	1	10	8.51	-9.4	71.06	366 ± 18	22.0 ± 1.1	-1.1 ± 2.9	8.3 ± 2.9	-9 ± 10	20 ± 8	-0.05 ± 0.06	0.12 ± 0.05
	3	18	3.93	-12.3	32.84	196 ± 9	11.8 ± 0.5	1.5 ± 1.3	13.8 ± 1.4	-4 ± 5	-5 ± 3	-0.05 ± 0.06	-0.06 ± 0.03
0238-084	1	20	13.93	64.3	1.45	486 ± 31	0.2 ± 0.0	74.9 ± 3.0	10.6 ± 3.0	-30 ± 41	11 ± 34	-0.06 ± 0.08	0.02 ± 0.07
	3	35	13.25	63.6	1.38	820 ± 21	0.3 ± 0.0	63.4 ± 1.1	0.2 ± 1.1	-26 ± 10	-3 ± 8	-0.03 ± 0.01	-0.00 ± 0.01
	7	18	6.11	67.0	0.63	1199 ± 21	0.4 ± 0.0	68.1 ± 0.8	1.1 ± 0.9	7 ± 28	-93 ± 22	0.01 ± 0.02	-0.08 ± 0.02
	8	19	5.74	68.2	0.60	1097 ± 16	0.4 ± 0.0	70.8 ± 1.3	2.6 ± 1.4	82 ± 19	-69 ± 30	0.08 ± 0.02	-0.06 ± 0.03
	9	27	6.62	68.3	0.69	981 ± 14	0.3 ± 0.0	69.2 ± 0.5	0.9 ± 0.6	-23 ± 8	-37 ± 5	-0.02 ± 0.01	-0.04 ± 0.01
	10	18	3.77	66.2	0.39	972 ± 21	0.3 ± 0.0	68.3 ± 1.0	2.1 ± 1.1	194 ± 30	6 ± 24	0.20 ± 0.03	0.01 ± 0.03
	11	11	2.24	65.2	0.23	468 ± 42	0.2 ± 0.0	64.4 ± 3.6	0.8 ± 3.7	31 ± 85	9 ± 60	0.07 ± 0.18	0.02 ± 0.13





Table 1 — *Continued*

Source (1)	I.D. (2)	N (3)	$\langle R \rangle$ (mas) (4)	$\langle \theta \rangle$ (deg.) (5)	$d_{proj}$ (pc) (6)	$\mu$ ( $\mu\text{as yr}^{-1}$ ) (7)	$\beta_{obs}$ (8)	$\phi$ (deg.) (9)	$ \langle \theta \rangle - \phi $ (deg.) (10)	$\dot{\mu}_{  }$ ( $\mu\text{as yr}^{-2}$ ) (11)	$\dot{\mu}_{\perp}$ ( $\mu\text{as yr}^{-2}$ ) (12)	$\dot{\eta}_{  }$ ( $\text{yr}^{-1}$ ) (13)	$\dot{\eta}_{\perp}$ ( $\text{yr}^{-1}$ ) (14)
0738+313	2	17	4.73	155.7	32.31	255 ± 12	9.3 ± 0.4	126.5 ± 2.5	29.2 ± 2.5	-16 ± 5	5 ± 5	-0.10 ± 0.04	0.03 ± 0.03
	3	21	3.97	160.5	27.12	165 ± 4	6.0 ± 0.1	118.3 ± 1.0	42.2 ± 1.1	-2 ± 2	-1 ± 1	-0.02 ± 0.02	-0.01 ± 0.01
	4	20	3.69	173.4	25.20	112 ± 4	4.1 ± 0.2	132.9 ± 2.1	40.5 ± 2.2	-4 ± 2	-7 ± 2	-0.05 ± 0.03	-0.10 ± 0.03
	6	21	3.38	177.7	23.08	89 ± 3	3.2 ± 0.1	155.9 ± 1.3	21.8 ± 1.3	-8 ± 1	-5 ± 1	-0.14 ± 0.03	-0.09 ± 0.02
	8	17	1.51	-176.0	10.28	161 ± 4	5.8 ± 0.2	-177.2 ± 0.6	1.3 ± 0.7	4 ± 2	-4 ± 1	0.04 ± 0.02	-0.04 ± 0.01
0748+126	2	16	4.29	117.6	33.41	304 ± 12	14.6 ± 0.6	120.5 ± 1.9	2.9 ± 1.9	-45 ± 7	-3 ± 6	-0.28 ± 0.04	-0.02 ± 0.04
	3	16	2.68	113.2	20.89	209 ± 7	10.0 ± 0.3	110.7 ± 1.4	2.5 ± 1.5	-8 ± 4	9 ± 3	-0.07 ± 0.03	0.09 ± 0.03
0754+100	13	10	2.89	22.4	11.75	632 ± 22	10.6 ± 0.4	12.7 ± 1.4	9.7 ± 1.4	-391 ± 40	-224 ± 27	-0.78 ± 0.08	-0.45 ± 0.06
0805-077	3	15	2.91	-27.9	24.80	529 ± 13	41.8 ± 1.1	-25.6 ± 0.9	2.3 ± 1.0	-66 ± 15	23 ± 10	-0.35 ± 0.08	0.12 ± 0.05
0823+033	7	16	2.11	28.0	12.89	429 ± 16	12.9 ± 0.5	26.9 ± 1.5	1.0 ± 1.6	-89 ± 15	-10 ± 10	-0.31 ± 0.05	-0.03 ± 0.03
	9	12	1.02	33.2	6.22	340 ± 20	10.2 ± 0.6	36.7 ± 2.6	3.5 ± 3.0	1 ± 28	33 ± 21	0.00 ± 0.12	0.15 ± 0.10
0827+243	2	23	2.29	123.6	18.14	367 ± 7	18.4 ± 0.4	139.1 ± 1.1	15.4 ± 1.2	-11 ± 5	7 ± 5	-0.06 ± 0.03	0.04 ± 0.03
	3	13	0.88	112.9	6.99	395 ± 25	19.8 ± 1.3	115.4 ± 4.1	2.5 ± 4.6	51 ± 36	37 ± 38	0.25 ± 0.18	0.18 ± 0.19
	4	13	1.07	110.2	8.48	390 ± 8	19.6 ± 0.4	117.9 ± 0.9	7.7 ± 1.1	-19 ± 12	54 ± 10	-0.09 ± 0.06	0.27 ± 0.05
0829+046	5	16	2.56	69.4	7.48	905 ± 31	10.1 ± 0.3	67.2 ± 2.1	2.2 ± 2.4	58 ± 36	-35 ± 38	0.07 ± 0.05	-0.05 ± 0.05
	6	14	2.54	67.6	7.44	754 ± 29	8.4 ± 0.3	69.4 ± 1.2	1.8 ± 1.4	7 ± 38	-41 ± 19	0.01 ± 0.06	-0.06 ± 0.03
0836+710	1	19	12.93	-149.5	108.24	222 ± 9	19.5 ± 0.7	-159.4 ± 1.1	9.9 ± 1.1	-12 ± 4	2 ± 2	-0.17 ± 0.06	0.04 ± 0.03
	2	15	8.65	-142.7	72.42	193 ± 19	17.0 ± 1.7	-148.2 ± 4.3	5.4 ± 4.3	-1 ± 11	4 ± 9	-0.01 ± 0.19	0.07 ± 0.15
	3	16	3.43	-145.8	28.74	145 ± 10	12.8 ± 0.8	-152.2 ± 2.6	6.4 ± 2.7	-11 ± 6	1 ± 4	-0.24 ± 0.13	0.03 ± 0.09
	4	18	2.28	-143.0	19.11	191 ± 5	16.8 ± 0.4	-149.6 ± 1.1	6.6 ± 1.2	-8 ± 2	-1 ± 2	-0.13 ± 0.04	-0.03 ± 0.03
	5	16	1.58	-139.5	13.24	216 ± 7	19.0 ± 0.6	-144.2 ± 1.8	4.7 ± 2.0	-9 ± 4	-2 ± 4	-0.14 ± 0.06	-0.04 ± 0.06
	6	15	1.02	-139.8	8.50	202 ± 7	17.7 ± 0.6	-139.3 ± 1.8	0.5 ± 2.2	7 ± 4	-3 ± 4	0.12 ± 0.06	-0.05 ± 0.06
0838+133	1	14	3.96	79.2	27.94	246 ± 8	9.5 ± 0.3	79.8 ± 3.6	0.6 ± 3.7	9 ± 4	-17 ± 7	0.06 ± 0.03	-0.12 ± 0.05
	2	15	3.14	79.4	22.15	246 ± 4	9.5 ± 0.1	94.0 ± 2.7	14.7 ± 2.8	4 ± 2	9 ± 7	0.03 ± 0.01	0.06 ± 0.05
	3	18	2.56	77.5	18.10	244 ± 7	9.5 ± 0.3	90.9 ± 2.2	13.4 ± 2.2	-24 ± 7	32 ± 9	-0.16 ± 0.05	0.22 ± 0.06
	5	15	1.47	83.5	10.38	278 ± 11	10.7 ± 0.4	80.2 ± 3.0	3.4 ± 3.3	10 ± 12	12 ± 16	0.06 ± 0.07	0.07 ± 0.10
0851+202	1	20	1.30	-94.5	5.81	580 ± 23	11.1 ± 0.4	-98.7 ± 1.5	4.2 ± 1.6	-106 ± 52	-172 ± 34	-0.24 ± 0.12	-0.39 ± 0.08
	5	18	1.15	-116.3	5.17	538 ± 7	10.3 ± 0.1	-103.0 ± 0.4	13.3 ± 0.4	-136 ± 24	117 ± 13	-0.33 ± 0.06	0.28 ± 0.03
	10	87	0.36	-125.5	1.60	23 ± 2	0.4 ± 0.0	-164.2 ± 3.9	38.7 ± 4.0	-1 ± 1	-4 ± 1	-0.08 ± 0.06	-0.21 ± 0.05
	15	24	3.34	-109.3	14.98	270 ± 20	5.1 ± 0.4	-111.2 ± 4.4	1.9 ± 4.4	-7 ± 30	33 ± 31	-0.03 ± 0.15	0.16 ± 0.15
0906+015	5	16	2.06	42.3	16.68	371 ± 6	19.8 ± 0.3	41.6 ± 0.8	0.7 ± 0.9	-5 ± 5	-2 ± 5	-0.03 ± 0.03	-0.01 ± 0.03
	7	13	1.38	44.7	11.19	413 ± 9	22.1 ± 0.5	44.8 ± 1.2	0.0 ± 1.4	12 ± 13	6 ± 13	0.06 ± 0.06	0.03 ± 0.06
0917+449	3	14	1.55	178.2	12.96	20 ± 3	1.7 ± 0.2	175.4 ± 3.4	2.8 ± 3.5	3 ± 1	-1 ± 1	0.47 ± 0.24	-0.22 ± 0.09
0917+624	3	21	2.70	-13.9	23.05	149 ± 14	10.1 ± 0.9	-17.3 ± 2.4	3.5 ± 2.5	-2 ± 6	-4 ± 3	-0.03 ± 0.10	-0.07 ± 0.05
	5	11	0.89	-31.7	7.63	135 ± 8	9.2 ± 0.6	-15.3 ± 2.8	16.4 ± 2.9	-5 ± 10	-36 ± 8	-0.08 ± 0.19	-0.66 ± 0.15
0923+392	2	32	2.94	100.9	20.95	39 ± 1	1.5 ± 0.1	91.7 ± 1.9	9.2 ± 1.9	1 ± 1	0 ± 1	0.02 ± 0.04	0.01 ± 0.03
0945+408	1	15	11.57	113.4	97.13	174 ± 12	10.7 ± 0.7	109.2 ± 3.7	4.2 ± 3.7	-22 ± 5	-0 ± 5	-0.28 ± 0.07	-0.00 ± 0.06
	2	15	8.50	118.2	71.41	149 ± 22	9.2 ± 1.4	85.6 ± 4.2	32.6 ± 4.3	-20 ± 8	4 ± 5	-0.30 ± 0.13	0.06 ± 0.08
	4	14	1.55	115.3	13.05	230 ± 7	14.2 ± 0.4	118.7 ± 1.5	3.4 ± 1.7	12 ± 4	6 ± 3	0.12 ± 0.04	0.06 ± 0.03
	5	12	1.50	131.2	12.55	290 ± 8	17.9 ± 0.5	131.7 ± 1.4	0.4 ± 1.6	-3 ± 6	3 ± 5	-0.03 ± 0.04	0.02 ± 0.04
0954+658	9	13	2.15	-51.0	10.91	565 ± 37	12.7 ± 0.8	-58.5 ± 3.2	7.5 ± 3.4	-183 ± 53	-37 ± 45	-0.44 ± 0.13	-0.09 ± 0.11
	11	10	0.68	-33.7	3.45	346 ± 20	7.8 ± 0.5	-40.0 ± 3.4	6.3 ± 3.8	37 ± 44	-37 ± 43	0.15 ± 0.17	-0.14 ± 0.17
1036+054	2	13	0.89	-5.4	5.26	202 ± 15	5.7 ± 0.4	-5.5 ± 1.1	0.2 ± 1.2	18 ± 11	10 ± 3	0.13 ± 0.08	0.08 ± 0.02
1127-145	2	12	5.90	77.5	49.11	236 ± 10	14.0 ± 0.6	58.8 ± 2.4	18.7 ± 2.4	-15 ± 7	-0 ± 7	-0.14 ± 0.06	-0.00 ± 0.07
	3	19	4.32	83.3	35.99	34 ± 3	2.0 ± 0.2	70.4 ± 4.1	13.0 ± 4.1	-5 ± 2	-4 ± 1	-0.31 ± 0.11	-0.25 ± 0.08
	4	17	4.38	80.9	36.45	221 ± 14	13.1 ± 0.8	81.1 ± 1.7	0.2 ± 1.7	-15 ± 7	-2 ± 4	-0.15 ± 0.07	-0.02 ± 0.04
	5	17	0.63	88.3	5.25	55 ± 8	3.2 ± 0.5	76.9 ± 4.2	11.4 ± 4.4	17 ± 5	-2 ± 3	0.67 ± 0.23	-0.08 ± 0.11
	8	10	2.07	86.7	17.22	251 ± 13	14.9 ± 0.8	91.5 ± 1.9	4.8 ± 2.1	8 ± 10	8 ± 6	0.07 ± 0.09	0.07 ± 0.05
1150+812	2	14	3.12	169.3	26.20	120 ± 6	7.4 ± 0.4	155.1 ± 3.3	14.2 ± 3.4	6 ± 2	-5 ± 3	0.12 ± 0.04	-0.10 ± 0.05
	3	14	2.70	178.6	22.70	110 ± 4	6.7 ± 0.2	161.7 ± 1.9	16.9 ± 2.0	5 ± 2	-7 ± 2	0.11 ± 0.03	-0.15 ± 0.03
	4	14	1.57	-165.9	13.15	164 ± 9	10.1 ± 0.5	172.4 ± 2.3	21.7 ± 2.5	22 ± 4	-14 ± 3	0.31 ± 0.06	-0.19 ± 0.04
	5	13	0.89	-144.9	7.49	100 ± 10	6.2 ± 0.6	-161.6 ± 3.9	16.6 ± 4.2	4 ± 5	-8 ± 3	0.08 ± 0.10	-0.18 ± 0.07
	6	12	0.42	-145.9	3.54	109 ± 4	6.7 ± 0.2	-153.8 ± 1.4	7.9 ± 1.7	26 ± 3	3 ± 2	0.54 ± 0.06	0.06 ± 0.04
1156+295	4	14	0.65	-2.4	4.73	302 ± 36	12.3 ± 1.5	2.8 ± 3.6	5.2 ± 4.0	144 ± 69	-78 ± 37	0.82 ± 0.41	-0.44 ± 0.22
1219+285	4	11	10.90	116.2	20.39	1356 ± 118	9.1 ± 0.8	139.8 ± 4.5	23.6 ± 4.6	440 ± 365	152 ± 331	0.36 ± 0.30	0.12 ± 0.27
	7	11	5.00	114.5	9.36	1061 ± 108	7.1 ± 0.7	105.7 ± 2.5	8.9 ± 2.6	629 ± 265	-286 ± 134	0.65 ± 0.28	-0.30 ± 0.14
	8	11	8.41	111.5	15.73	848 ± 37	5.7 ± 0.2	122.0 ± 2.6	10.4 ± 2.6	-75 ± 45	165 ± 47	-0.10 ± 0.06	0.21 ± 0.06
	9	10	4.95	108.3	9.26	766 ± 58	5.2 ± 0.4	107.5 ± 3.4	0.8 ± 3.5	44 ± 73	-178 ± 58	0.06 ± 0.11	-0.26 ± 0.09
	15	22	4.86	108.9	9.09	475 ± 16	3.2 ± 0.1	116.0 ± 1.6	7.1 ± 1.7	-102 ± 15	14 ± 12	-0.24 ± 0.04	0.03 ± 0.03
1222+216	1	24	13.50	-5.9	75.78	320 ± 9	8.4 ± 0.2	11.5 ± 1.4	17.4 ± 1.4	-9 ± 5	11 ± 4	-0.04 ± 0.02	0.05 ± 0.02
	2	17	7.40	7.4	41.53	581 ± 17	15.3 ± 0.4	15.7 ± 1.2	8.2 ± 1.2	-3 ± 11	37 ± 8	-0.01 ± 0.03	0.09 ± 0.02
	3	13	3.67	2.7	20.59	641 ± 8	16.8 ± 0.2	10.2 ± 0.3	7.5 ± 0.3	2 ± 7	33 ± 2	0.00 ± 0.02	0.07 ± 0.01
	4	25	5.34	4.3	29.95	639 ± 5	16.8 ± 0.1	9.7 ± 0.4	5.4 ± 0.5	4 ± 3	26 ± 2	0.01 ± 0.01	0.06 ± 0.01
	5	20	5.25	-0.5	29.47	631 ± 6	16.6 ± 0.2	5.7 ± 0.2	6.2 ± 0.2	-10 ± 4	33 ± 1	-0.02 ± 0.01	0.07 ± 0.00
	6	16	5.08	-4.2	28.50	779 ± 15	20.5 ± 0.4	-6.8 ± 1.0	2.6 ± 1.1	7 ± 14	-22 ± 11	0.01 ± 0.03	-0.04 ± 0.02
	7	14	4.07	4.5	22.85	1013 ± 39	26.6 ± 1.0	3.0 ± 0.9	1.5 ± 1.1	221 ± 55	-74 ± 23	0.31 ± 0.08	-0.11 ± 0.03
	9	10	2.14	0.9	12.04	632 ± 45	16.6 ± 1.2	0.2 ± 0.9	0.7 ± 0.9	103 ± 68	5 ± 17	0.23 ± 0.15	0.01 ± 0.04
1226+023	1	16	18.62	-123.8	50.40	829 ± 45	8.5 ± 0.5	-143.9 ± 3.0	20.1 ± 3.0	199 ± 81	77 ± 74	0.28 ± 0.11	0.11 ± 0.10
	2	60	14.49	-123.0	39.22	784 ± 5	8.0 ± 0.1	-131.4 ± 0.4	8.4 ± 0.4	48 ± 3	-32 ± 3	0.07 ± 0.00	-0.05 ± 0.00
	3	22	6.36	-113.6	17.21	1026 ± 15	10.5 ± 0.2	-119.2 ± 0.6	5.5 ± 0.6	-103 ± 27	-34 ± 19	-0.12 ± 0.03	-0.04 ± 0.02
	4	10	2.48	-114.6	6.72	1255 ± 54	12.8 ± 0.6	-114.3 ± 2.7	0.3 ± 2.7	532 ± 237	-297 ± 243	0.49 ± 0.22	-0.27 ± 0.22
	5	23	4.11	-117.3	11.13	1455 ± 16	14.9 ± 0.2	-114.8 ± 0.6	2.5 ± 0.7	25 ± 29	44 ± 28	0.02 ± 0.02	0.04 ± 0.02
	9	54	6.80	-125.5	18.41	1013 ± 7	10.4 ± 0.1	-120.1 ± 0.4	5.4 ± 0.4	37 ± 4	70 ± 4	0.04 ± 0.01	0.08 ± 0.01
	12	43	4.14	-132.2	11.21	887 ± 8	9.1 ± 0.1	-127.6 ± 0.5	4.6 ± 0.6	3 ± 8	79 ± 8	0.00 ± 0.01	0.10 ± 0.01

Table 1 — *Continued*

Source (1)	I.D. (2)	N (3)	$\langle R \rangle$ (mas) (4)	$\langle \theta \rangle$ (deg.) (5)	$d_{proj}$ (pc) (6)	$\mu$ ( $\mu\text{as yr}^{-1}$ ) (7)	$\beta_{obs}$ (8)	$\phi$ (deg.) (9)	$ \langle \theta \rangle - \phi $ (deg.) (10)	$\dot{\mu}_{  }$ ( $\mu\text{as yr}^{-2}$ ) (11)	$\dot{\mu}_{\perp}$ ( $\mu\text{as yr}^{-2}$ ) (12)	$\dot{\eta}_{  }$ ( $\text{yr}^{-1}$ ) (13)	$\dot{\eta}_{\perp}$ ( $\text{yr}^{-1}$ ) (14)
	13	14	1.41	-110.8	3.82	600 ± 28	6.1 ± 0.3	-117.5 ± 3.5	6.7 ± 3.7	28 ± 85	-126 ± 109	0.05 ± 0.16	-0.24 ± 0.21
	15	13	1.72	-141.4	4.67	849 ± 25	8.7 ± 0.3	-140.1 ± 1.6	1.3 ± 1.8	148 ± 62	-52 ± 62	0.20 ± 0.08	-0.07 ± 0.08
	16	10	1.40	-142.6	3.79	611 ± 33	6.2 ± 0.3	-140.2 ± 3.0	2.4 ± 3.1	-650 ± 128	219 ± 126	-1.23 ± 0.25	0.42 ± 0.24
	19	17	4.61	-138.9	12.46	713 ± 33	7.3 ± 0.3	-122.9 ± 1.9	16.0 ± 1.9	-186 ± 86	258 ± 61	-0.30 ± 0.14	0.42 ± 0.10
	21	24	4.31	-123.7	11.67	538 ± 15	5.5 ± 0.2	-101.7 ± 2.3	22.0 ± 2.3	25 ± 23	45 ± 35	0.05 ± 0.05	0.10 ± 0.08
	24	14	1.27	-139.9	3.43	716 ± 24	7.3 ± 0.3	-136.7 ± 2.0	3.3 ± 2.0	289 ± 99	78 ± 98	0.47 ± 0.16	0.13 ± 0.16
	25	14	0.77	-147.8	2.10	513 ± 26	5.2 ± 0.3	-140.6 ± 2.7	7.2 ± 2.8	762 ± 118	-44 ± 110	1.72 ± 0.28	-0.10 ± 0.25
	26	44	12.94	-119.2	35.02	878 ± 5	9.0 ± 0.1	-128.6 ± 0.4	9.4 ± 0.4	8 ± 4	-25 ± 5	0.01 ± 0.01	-0.03 ± 0.01
	27	12	3.80	-120.6	10.28	1206 ± 49	12.3 ± 0.5	-124.8 ± 2.1	4.2 ± 2.2	-502 ± 119	-250 ± 109	-0.48 ± 0.12	-0.24 ± 0.11
	29	17	2.72	-143.2	7.36	928 ± 33	9.5 ± 0.3	-147.3 ± 1.7	4.1 ± 1.8	-303 ± 85	403 ± 73	-0.38 ± 0.11	0.50 ± 0.09
1253-055	1	115	4.73	-122.2	29.85	348 ± 2	11.0 ± 0.1	-138.1 ± 0.3	15.9 ± 0.4	1 ± 1	1 ± 1	0.00 ± 0.00	0.00 ± 0.00
	2	47	3.26	-118.5	20.59	254 ± 12	8.0 ± 0.4	-114.2 ± 2.0	4.3 ± 2.0	-38 ± 22	31 ± 15	-0.23 ± 0.13	0.19 ± 0.09
	6	46	1.44	-127.2	9.11	493 ± 9	15.6 ± 0.3	-127.5 ± 1.1	0.3 ± 1.1	353 ± 19	34 ± 18	1.10 ± 0.06	0.11 ± 0.06
	7	28	1.42	-125.5	8.97	651 ± 25	20.6 ± 0.8	-120.8 ± 1.9	4.8 ± 2.0	27 ± 64	48 ± 56	0.06 ± 0.15	0.11 ± 0.13
	8	16	0.94	-134.7	5.94	304 ± 17	9.6 ± 0.5	-113.4 ± 3.3	21.3 ± 3.4	363 ± 70	204 ± 72	1.83 ± 0.37	1.03 ± 0.37
	10	23	1.42	-133.8	8.97	516 ± 13	16.3 ± 0.4	-127.6 ± 1.3	6.2 ± 1.6	45 ± 19	42 ± 18	0.13 ± 0.06	0.12 ± 0.05
1308+326	1	24	10.85	-79.5	87.21	444 ± 18	23.2 ± 0.9	-89.1 ± 2.5	9.6 ± 2.6	-24 ± 14	24 ± 16	-0.11 ± 0.07	0.11 ± 0.07
	2	48	3.43	-73.3	27.56	407 ± 8	21.3 ± 0.4	-73.2 ± 0.7	0.1 ± 0.8	-1 ± 4	-1 ± 3	-0.01 ± 0.02	-0.01 ± 0.01
	3	13	1.69	-63.6	13.60	442 ± 46	23.2 ± 2.4	-75.8 ± 3.3	12.2 ± 3.5	132 ± 69	-85 ± 42	0.60 ± 0.32	-0.38 ± 0.19
	4	22	1.81	-51.4	14.52	525 ± 22	27.5 ± 1.2	-64.7 ± 1.4	13.3 ± 1.6	-34 ± 40	17 ± 24	-0.13 ± 0.15	0.06 ± 0.09
	5	18	2.45	-42.0	19.71	402 ± 6	21.0 ± 0.3	-50.3 ± 0.8	8.3 ± 0.8	7 ± 16	-23 ± 17	0.04 ± 0.08	-0.11 ± 0.08
	7	16	1.84	-61.9	14.79	340 ± 30	17.8 ± 1.6	-63.7 ± 4.0	1.8 ± 4.2	-105 ± 44	34 ± 39	-0.62 ± 0.26	0.20 ± 0.23
	8	16	1.32	-57.5	10.62	202 ± 20	10.6 ± 1.0	-74.0 ± 3.3	16.5 ± 3.4	-85 ± 32	72 ± 19	-0.84 ± 0.33	0.72 ± 0.20
	9	13	0.32	-28.9	2.56	160 ± 5	8.4 ± 0.3	-34.2 ± 1.8	5.3 ± 1.9	117 ± 18	-22 ± 18	1.47 ± 0.23	-0.28 ± 0.23
	11	16	3.78	-48.3	30.37	350 ± 9	18.3 ± 0.5	-83.5 ± 1.1	35.2 ± 1.1	-5 ± 15	-79 ± 11	-0.03 ± 0.09	-0.45 ± 0.07
1334-127	5	10	2.19	145.6	13.85	482 ± 25	15.3 ± 0.8	153.5 ± 2.3	7.9 ± 2.5	9 ± 32	19 ± 25	0.03 ± 0.10	0.06 ± 0.08
	9	10	0.95	144.2	6.04	343 ± 14	10.9 ± 0.4	158.3 ± 2.0	14.1 ± 2.3	20 ± 29	33 ± 25	0.09 ± 0.13	0.15 ± 0.11
1406-076	2	14	7.38	-106.5	62.98	259 ± 9	18.0 ± 0.6	-113.4 ± 2.6	6.9 ± 2.7	23 ± 8	-16 ± 11	0.23 ± 0.08	-0.16 ± 0.10
	11	11	1.92	-109.6	16.41	260 ± 13	18.1 ± 0.9	-109.0 ± 2.9	0.6 ± 2.9	-58 ± 28	24 ± 28	-0.55 ± 0.27	0.23 ± 0.27
1413+135	3	17	7.15	-111.0	27.46	114 ± 7	1.8 ± 0.1	-107.1 ± 4.2	3.9 ± 4.2	-13 ± 3	-6 ± 4	-0.15 ± 0.04	-0.07 ± 0.04
1458+718	2	12	27.17	166.3	212.56	95 ± 22	4.6 ± 1.1	0.5 ± 3.2	165.9 ± 3.2	16 ± 11	-5 ± 3	0.33 ± 0.23	-0.09 ± 0.06
	6	13	1.54	162.8	12.03	136 ± 6	6.6 ± 0.3	163.3 ± 1.5	0.5 ± 1.6	-1 ± 3	1 ± 2	-0.01 ± 0.05	0.01 ± 0.03
	7	12	1.22	159.6	9.55	127 ± 6	6.2 ± 0.3	161.0 ± 1.7	1.5 ± 1.8	-7 ± 3	-0 ± 2	-0.10 ± 0.04	-0.00 ± 0.03
1502+106	2	20	2.49	122.5	21.25	131 ± 7	10.4 ± 0.5	116.3 ± 2.5	6.1 ± 2.5	4 ± 3	-0 ± 3	0.08 ± 0.07	-0.01 ± 0.06
	4	11	0.86	100.1	7.34	222 ± 11	17.6 ± 0.9	101.0 ± 1.6	0.9 ± 1.7	34 ± 12	25 ± 7	0.44 ± 0.16	0.32 ± 0.09
1510-089	1	18	3.22	-25.5	16.08	711 ± 18	15.8 ± 0.4	-25.6 ± 0.9	0.1 ± 1.0	-96 ± 22	2 ± 14	-0.18 ± 0.04	0.00 ± 0.03
	4	10	2.02	-34.8	10.10	908 ± 48	20.1 ± 1.1	-33.9 ± 3.3	0.9 ± 3.7	121 ± 79	-14 ± 88	0.18 ± 0.12	-0.02 ± 0.13
	8	26	3.65	-28.3	18.24	1042 ± 22	23.1 ± 0.5	-25.3 ± 1.3	3.0 ± 1.4	88 ± 24	29 ± 26	0.11 ± 0.03	0.04 ± 0.03
	15	22	0.97	-33.7	4.87	788 ± 20	17.5 ± 0.5	-33.8 ± 1.1	0.1 ± 1.4	386 ± 60	-118 ± 46	0.67 ± 0.11	-0.20 ± 0.08
	16	18	1.59	-36.1	7.97	1263 ± 27	28.0 ± 0.6	-33.0 ± 1.3	3.0 ± 1.5	752 ± 73	96 ± 74	0.81 ± 0.08	0.10 ± 0.08
1514-241	8	10	6.90	163.5	6.53	1863 ± 105	6.0 ± 0.3	155.3 ± 1.8	8.2 ± 1.8	-237 ± 194	-73 ± 109	-0.13 ± 0.11	-0.04 ± 0.06
	9	14	7.00	165.1	6.62	1981 ± 60	6.4 ± 0.2	157.1 ± 1.2	8.1 ± 1.2	-520 ± 109	-391 ± 74	-0.28 ± 0.06	-0.21 ± 0.04
1546+027	3	10	2.30	172.1	12.56	438 ± 25	11.0 ± 0.6	168.4 ± 2.5	3.7 ± 2.8	4 ± 26	-13 ± 19	0.01 ± 0.08	-0.04 ± 0.06
	4	10	1.06	173.0	5.76	166 ± 22	4.2 ± 0.6	166.0 ± 3.5	7.0 ± 3.7	-13 ± 22	-13 ± 10	-0.11 ± 0.19	-0.11 ± 0.09
	6	13	1.40	167.4	7.63	364 ± 11	9.2 ± 0.3	162.8 ± 0.9	4.6 ± 1.0	83 ± 14	-32 ± 8	0.32 ± 0.06	-0.12 ± 0.03
	7	10	0.92	-168.5	5.01	382 ± 11	9.6 ± 0.3	-170.9 ± 1.2	2.4 ± 1.3	191 ± 21	24 ± 15	0.71 ± 0.08	0.09 ± 0.06
1606+106	7	12	1.83	-46.2	15.34	313 ± 14	19.1 ± 0.9	-34.2 ± 2.4	12.1 ± 2.6	3 ± 10	2 ± 9	0.02 ± 0.07	0.01 ± 0.07
1611+343	4	33	2.99	170.8	25.41	71 ± 3	4.7 ± 0.2	115.4 ± 1.9	55.4 ± 1.9	5 ± 1	2 ± 1	0.18 ± 0.04	0.07 ± 0.04
1633+382	2	23	2.13	-90.0	18.16	256 ± 13	20.0 ± 1.0	-93.0 ± 0.9	3.0 ± 1.0	-10 ± 11	-16 ± 4	-0.11 ± 0.12	-0.17 ± 0.04
	3	19	1.56	-74.8	13.30	286 ± 15	22.4 ± 1.1	-65.8 ± 4.1	9.0 ± 4.4	-57 ± 19	-36 ± 27	-0.56 ± 0.19	-0.36 ± 0.26
	4	16	1.08	-90.1	9.25	373 ± 16	29.3 ± 1.3	-90.0 ± 1.0	0.1 ± 1.2	-46 ± 23	12 ± 11	-0.34 ± 0.17	0.09 ± 0.08
	5	14	0.90	-79.9	7.66	292 ± 13	22.9 ± 1.0	-83.8 ± 1.8	3.9 ± 1.9	-109 ± 24	-3 ± 16	-1.05 ± 0.23	-0.03 ± 0.16
	8	18	1.75	-77.0	14.91	104 ± 13	8.1 ± 1.0	-89.2 ± 3.0	12.2 ± 3.0	-53 ± 17	23 ± 7	-1.43 ± 0.48	0.61 ± 0.20
1637+574	1	12	4.31	-159.3	31.68	213 ± 10	8.9 ± 0.4	-149.3 ± 2.6	10.0 ± 2.6	-28 ± 8	11 ± 9	-0.23 ± 0.07	0.09 ± 0.07
	2	13	3.66	-158.3	26.92	306 ± 16	12.8 ± 0.7	-156.8 ± 3.1	1.6 ± 3.2	22 ± 16	21 ± 14	0.12 ± 0.09	0.12 ± 0.08
	6	10	0.91	-151.9	6.67	228 ± 16	9.6 ± 0.7	-159.4 ± 2.2	7.5 ± 2.4	99 ± 22	-27 ± 12	0.76 ± 0.18	-0.21 ± 0.09
1641+399	1	30	7.35	-69.6	48.77	261 ± 24	9.0 ± 0.8	-59.9 ± 4.6	9.7 ± 4.7	12 ± 20	-4 ± 17	0.07 ± 0.12	-0.02 ± 0.11
	2	34	5.21	-78.2	34.57	253 ± 11	8.7 ± 0.4	-58.8 ± 2.7	19.4 ± 2.8	-37 ± 7	10 ± 8	-0.24 ± 0.05	0.07 ± 0.05
	3	39	3.06	-91.7	20.33	320 ± 8	11.0 ± 0.3	-74.0 ± 1.1	17.7 ± 1.1	3 ± 5	42 ± 4	0.01 ± 0.03	0.21 ± 0.02
	5	13	1.19	-89.6	7.90	408 ± 23	14.1 ± 0.8	-78.8 ± 1.5	10.8 ± 1.6	236 ± 54	-35 ± 25	0.92 ± 0.22	-0.14 ± 0.10
	6	41	2.17	-91.8	14.43	339 ± 4	11.7 ± 0.2	-84.5 ± 0.5	7.4 ± 0.6	-0 ± 3	9 ± 2	-0.00 ± 0.01	0.04 ± 0.01
	7	55	2.83	-95.0	18.77	368 ± 2	12.7 ± 0.1	-90.8 ± 0.5	4.2 ± 0.6	-0 ± 1	10 ± 2	-0.00 ± 0.01	0.04 ± 0.01
	8	47	2.44	-89.7	16.21	337 ± 3	11.6 ± 0.1	-89.9 ± 0.4	0.2 ± 0.5	10 ± 2	-10 ± 2	0.05 ± 0.01	-0.05 ± 0.01
	9	40	2.10	-94.8	13.95	349 ± 4	12.0 ± 0.1	-98.0 ± 0.4	3.3 ± 0.5	3 ± 3	1 ± 2	0.01 ± 0.02	0.00 ± 0.01
	11	18	0.98	-86.8	6.51	559 ± 15	19.3 ± 0.5	-87.8 ± 0.7	1.0 ± 0.8	73 ± 35	-16 ± 19	0.21 ± 0.10	-0.05 ± 0.05
	12	32	1.94	-91.7	12.86	382 ± 11	13.2 ± 0.4	-95.5 ± 0.8	3.8 ± 0.8	-39 ± 13	-37 ± 6	-0.16 ± 0.06	-0.15 ± 0.03
	13	28	1.30	-88.2	8.61	263 ± 10	9.1 ± 0.4	-83.0 ± 1.6	5.2 ± 1.7	-3 ± 15	16 ± 10	-0.02 ± 0.09	0.10 ± 0.06
	15	21	0.98	-90.3	6.54	321 ± 19	11.1 ± 0.6	-92.2 ± 1.6	1.9 ± 1.6	20 ± 43	-18 ± 20	0.10 ± 0.21	-0.09 ± 0.10
1642+690	3	13	3.43	-162.4	25.17	346 ± 6	14.5 ± 0.3	-162.6 ± 0.7	0.2 ± 0.8	-15 ± 4	2 ± 2	-0.08 ± 0.02	0.01 ± 0.01
1655+077	6	15	2.49	-36.7	16.91	337 ± 9	12.1 ± 0.3	-42.7 ± 1.5	6.0 ± 1.7	7 ± 5	-8 ± 4	0.04 ± 0.02	-0.04 ± 0.02
	7	11	1.84	-36.3	12.48	300 ± 16	10.8 ± 0.6	-35.7 ± 2.8	0.6 ± 3.1	-6 ± 11	4 ± 10	-0.03 ± 0.06	0.02 ± 0.05
1730-130	2	28	7.51	13.7	58.72	360 ± 14	17.5 ± 0.7	11.3 ± 1.4	2.4 ± 1.5	-39 ± 7	-12 ± 4	-0.21 ± 0.04	-0.06 ± 0.02
	4	15	4.91	5.3	38.40	564 ± 20	27.4 ± 1.0	2.6 ± 1.5	2.7 ± 1.6	-84 ± 22	-33 ± 16	-0.28 ± 0.07	-0.11 ± 0.05
	6	25	2.44	26.1	19.10	283 ± 8	13.7 ± 0.4	24.2 ± 1.1	2.0 ± 1.3	-13 ± 4	-5 ± 3	-0.09 ± 0.03	-0.03 ± 0.02

Table 1 — *Continued*

Source (1)	I.D. (2)	N (3)	$\langle R \rangle$ (mas) (4)	$\langle \theta \rangle$ (deg.) (5)	$d_{proj}$ (pc) (6)	$\mu$ ( $\mu\text{as yr}^{-1}$ ) (7)	$\beta_{obs}$ (8)	$\phi$ (deg.) (9)	$ \langle \theta \rangle - \phi $ (deg.) (10)	$\dot{\mu}_{  }$ ( $\mu\text{as yr}^{-2}$ ) (11)	$\dot{\mu}_{\perp}$ ( $\mu\text{as yr}^{-2}$ ) (12)	$\dot{\eta}_{  }$ ( $\text{yr}^{-1}$ ) (13)	$\dot{\eta}_{\perp}$ ( $\text{yr}^{-1}$ ) (14)
	7	15	1.89	9.6	14.80	184 ± 21	8.9 ± 1.0	-14.9 ± 4.3	24.5 ± 4.4	23 ± 21	25 ± 14	0.24 ± 0.22	0.26 ± 0.15
	8	18	1.36	-7.2	10.62	348 ± 13	16.9 ± 0.6	-10.9 ± 0.6	3.7 ± 0.7	85 ± 12	3 ± 4	0.46 ± 0.07	0.01 ± 0.02
1749+096	5	22	0.41	-2.2	1.89	121 ± 18	2.4 ± 0.4	22.3 ± 4.2	24.5 ± 4.3	141 ± 36	20 ± 18	1.54 ± 0.45	0.22 ± 0.20
1800+440	3	11	4.47	-162.1	31.20	396 ± 13	15.0 ± 0.5	-161.8 ± 2.7	0.3 ± 2.9	0 ± 8	3 ± 12	0.00 ± 0.04	0.01 ± 0.05
1803+784	1	22	6.52	-95.3	45.99	279 ± 32	10.8 ± 1.2	-92.3 ± 2.3	3.0 ± 2.3	29 ± 25	17 ± 8	0.18 ± 0.15	0.10 ± 0.05
1823+568	1	21	7.50	-160.9	52.41	234 ± 36	8.9 ± 1.4	-165.5 ± 4.5	4.6 ± 4.6	29 ± 40	-37 ± 20	0.21 ± 0.29	-0.26 ± 0.15
	2	36	6.58	-160.6	45.99	138 ± 15	5.2 ± 0.6	-150.9 ± 4.6	9.7 ± 4.6	22 ± 10	1 ± 7	0.27 ± 0.12	0.02 ± 0.09
	4	34	4.43	-159.2	30.99	496 ± 9	18.8 ± 0.4	-163.1 ± 0.8	3.9 ± 0.9	-26 ± 6	-6 ± 4	-0.09 ± 0.02	-0.02 ± 0.01
	6	17	1.72	-161.3	12.02	207 ± 8	7.9 ± 0.3	-167.5 ± 1.6	6.2 ± 1.6	-93 ± 14	24 ± 11	-0.75 ± 0.12	0.19 ± 0.09
	8	22	1.58	-160.5	11.01	153 ± 12	5.8 ± 0.5	-163.7 ± 2.7	3.2 ± 2.8	1 ± 11	5 ± 7	0.01 ± 0.12	0.06 ± 0.07
	12	22	1.97	-161.4	13.78	88 ± 7	3.3 ± 0.3	-153.8 ± 4.6	7.6 ± 4.6	-7 ± 10	-25 ± 9	-0.14 ± 0.19	-0.46 ± 0.18
1828+487	2	14	12.05	-34.8	85.72	281 ± 8	11.0 ± 0.3	-36.8 ± 1.6	2.0 ± 1.6	-26 ± 4	3 ± 4	-0.15 ± 0.03	0.02 ± 0.02
	3	14	10.96	-32.0	77.92	252 ± 4	9.9 ± 0.2	-40.0 ± 1.1	8.0 ± 1.1	-7 ± 2	-7 ± 2	-0.05 ± 0.01	-0.05 ± 0.02
	5	15	5.50	-28.5	39.08	332 ± 9	13.0 ± 0.3	-28.4 ± 1.0	0.1 ± 1.0	-5 ± 4	-5 ± 3	-0.03 ± 0.02	-0.03 ± 0.02
	6	11	2.50	-29.4	17.78	322 ± 11	12.7 ± 0.4	-31.4 ± 1.5	2.1 ± 1.6	-18 ± 9	-7 ± 7	-0.09 ± 0.05	-0.04 ± 0.04
	8	13	2.47	-37.7	17.58	333 ± 4	13.1 ± 0.1	-36.2 ± 0.6	1.5 ± 0.6	16 ± 2	6 ± 2	0.08 ± 0.01	0.03 ± 0.01
	10	12	1.32	-43.9	9.42	125 ± 10	4.9 ± 0.4	-46.1 ± 4.8	2.2 ± 5.0	35 ± 8	-4 ± 8	0.48 ± 0.11	-0.06 ± 0.11
1845+797	1	12	8.45	-35.2	8.99	661 ± 9	2.4 ± 0.0	-33.0 ± 0.8	2.2 ± 0.8	32 ± 5	-12 ± 5	0.05 ± 0.01	-0.02 ± 0.01
	3	14	7.25	-40.2	7.71	597 ± 18	2.2 ± 0.1	-38.8 ± 1.8	1.5 ± 1.9	4 ± 9	-17 ± 9	0.01 ± 0.02	-0.03 ± 0.02
	4	12	6.77	-38.8	7.20	406 ± 19	1.5 ± 0.1	-40.6 ± 2.6	1.9 ± 2.7	60 ± 18	4 ± 18	0.15 ± 0.05	0.01 ± 0.05
	5	12	6.83	-37.9	7.27	398 ± 32	1.5 ± 0.1	-38.3 ± 4.6	0.5 ± 4.6	-168 ± 66	49 ± 63	-0.44 ± 0.18	0.13 ± 0.17
1849+670	4	12	2.44	-44.2	16.98	614 ± 24	23.1 ± 0.9	-50.0 ± 2.2	5.7 ± 2.4	-149 ± 35	-1 ± 34	-0.40 ± 0.10	-0.00 ± 0.09
1928+738	1	39	12.19	167.5	54.13	433 ± 11	8.2 ± 0.2	-178.6 ± 0.7	13.9 ± 0.7	-6 ± 5	6 ± 2	-0.02 ± 0.02	0.02 ± 0.01
	2	13	6.26	165.1	27.81	400 ± 56	7.5 ± 1.1	173.1 ± 3.4	8.0 ± 3.4	-68 ± 67	-5 ± 29	-0.22 ± 0.22	-0.02 ± 0.10
	3	39	4.93	163.7	21.92	260 ± 8	4.9 ± 0.2	171.2 ± 1.2	7.5 ± 1.2	20 ± 4	-6 ± 2	0.10 ± 0.02	-0.03 ± 0.01
	4	16	3.23	170.4	14.35	349 ± 14	6.6 ± 0.3	174.7 ± 0.8	4.3 ± 0.8	8 ± 31	3 ± 12	0.03 ± 0.11	0.01 ± 0.04
	5	37	3.45	170.2	15.34	269 ± 8	5.1 ± 0.2	166.8 ± 0.7	3.3 ± 0.7	-9 ± 3	-1 ± 1	-0.04 ± 0.02	-0.01 ± 0.01
	6	30	2.66	159.7	11.82	255 ± 4	4.8 ± 0.1	171.5 ± 0.7	11.8 ± 0.7	-14 ± 3	28 ± 2	-0.07 ± 0.01	0.14 ± 0.01
	8	39	2.10	158.4	9.32	260 ± 4	4.9 ± 0.1	164.2 ± 0.3	5.8 ± 0.4	-1 ± 2	3 ± 1	-0.00 ± 0.01	0.02 ± 0.00
	9	30	1.42	151.3	6.30	244 ± 8	4.6 ± 0.1	151.3 ± 1.4	0.1 ± 1.6	4 ± 5	3 ± 4	0.02 ± 0.03	0.01 ± 0.02
	10	30	1.38	155.7	6.11	255 ± 5	4.8 ± 0.1	153.3 ± 0.9	2.4 ± 1.1	25 ± 3	-1 ± 3	0.13 ± 0.02	-0.00 ± 0.01
	11	29	0.85	157.2	3.76	160 ± 4	3.0 ± 0.1	155.3 ± 1.0	1.9 ± 1.2	12 ± 2	-1 ± 2	0.10 ± 0.02	-0.00 ± 0.02
	12	12	1.05	161.3	4.67	158 ± 17	3.0 ± 0.3	163.4 ± 2.4	2.1 ± 2.5	-22 ± 18	-6 ± 7	-0.18 ± 0.15	-0.05 ± 0.06
	13	11	0.68	159.1	3.04	134 ± 11	2.5 ± 0.2	155.9 ± 3.4	3.2 ± 3.7	-7 ± 13	-1 ± 9	-0.06 ± 0.13	-0.01 ± 0.09
1957+405	3	24	2.33	-79.4	2.50	72 ± 11	0.3 ± 0.0	-83.8 ± 2.4	4.4 ± 2.5	-8 ± 5	0 ± 1	-0.11 ± 0.08	0.00 ± 0.02
	4	24	1.57	-81.7	1.69	64 ± 8	0.2 ± 0.0	-94.2 ± 2.9	12.6 ± 2.9	-3 ± 4	0 ± 2	-0.05 ± 0.06	0.00 ± 0.03
	6	23	0.93	-82.6	1.00	45 ± 5	0.2 ± 0.0	-93.9 ± 3.7	11.3 ± 3.8	2 ± 2	3 ± 1	0.06 ± 0.05	0.06 ± 0.03
	10	24	1.03	106.1	1.10	38 ± 7	0.1 ± 0.0	110.0 ± 4.9	3.9 ± 4.9	6 ± 3	-1 ± 1	0.16 ± 0.10	-0.02 ± 0.04
2008-159	1	10	1.49	9.6	12.37	82 ± 12	4.9 ± 0.7	14.6 ± 2.7	5.0 ± 2.7	-20 ± 6	4 ± 2	-0.54 ± 0.17	0.11 ± 0.05
2013+370	2	12	1.49	-147.5	11.47	268 ± 7	12.5 ± 0.3	-147.7 ± 1.3	0.2 ± 1.4	58 ± 6	1 ± 5	0.40 ± 0.05	0.01 ± 0.04
2121+053	2	13	1.15	-63.8	9.82	143 ± 9	11.6 ± 0.7	-44.4 ± 3.6	19.4 ± 3.9	-4 ± 4	17 ± 4	-0.08 ± 0.09	0.36 ± 0.09
2128-123	3	12	5.74	-148.6	34.93	191 ± 10	5.7 ± 0.3	-154.8 ± 1.7	6.2 ± 1.8	3 ± 6	11 ± 3	0.02 ± 0.05	0.09 ± 0.03
	4	10	4.97	-148.2	30.29	201 ± 21	6.0 ± 0.6	-167.9 ± 4.0	19.8 ± 4.0	-12 ± 16	10 ± 10	-0.09 ± 0.12	0.08 ± 0.08
2131-021	1	14	1.50	101.8	12.61	195 ± 11	12.2 ± 0.7	99.0 ± 2.1	2.8 ± 2.3	-0 ± 8	18 ± 6	-0.01 ± 0.10	0.21 ± 0.07
	3	14	1.78	110.3	15.01	189 ± 5	11.9 ± 0.3	86.2 ± 2.1	24.1 ± 2.2	-18 ± 4	-21 ± 6	-0.21 ± 0.05	-0.25 ± 0.07
	4	17	0.89	97.8	7.49	49 ± 3	3.1 ± 0.2	79.0 ± 3.1	18.8 ± 3.1	-17 ± 2	0 ± 2	-0.80 ± 0.12	0.01 ± 0.09
2134+004	2	33	1.74	-67.6	14.80	62 ± 4	5.1 ± 0.3	-146.9 ± 3.4	79.3 ± 3.5	-5 ± 2	1 ± 2	-0.26 ± 0.08	0.05 ± 0.08
2136+141	3	15	0.84	-90.5	6.91	45 ± 2	4.1 ± 0.2	-132.9 ± 2.6	42.4 ± 2.7	-9 ± 1	-2 ± 1	-0.70 ± 0.08	-0.17 ± 0.08
	4	16	0.54	-74.7	4.47	34 ± 1	3.1 ± 0.1	-129.4 ± 2.4	54.7 ± 2.5	-4 ± 1	-2 ± 1	-0.43 ± 0.06	-0.21 ± 0.07
2155-152	3	14	1.36	-140.9	9.54	241 ± 11	9.2 ± 0.4	-135.8 ± 2.5	5.1 ± 2.6	-19 ± 11	-16 ± 11	-0.13 ± 0.08	-0.11 ± 0.08
2200+420	3	19	3.18	-167.8	4.12	930 ± 57	4.2 ± 0.3	179.4 ± 1.5	12.7 ± 1.6	578 ± 172	-156 ± 75	0.66 ± 0.20	-0.18 ± 0.09
	4	40	4.02	-177.5	5.21	1332 ± 47	6.0 ± 0.2	156.8 ± 1.7	25.7 ± 1.9	366 ± 69	-308 ± 59	0.29 ± 0.06	-0.25 ± 0.05
	5	37	2.47	-165.1	3.20	778 ± 29	3.5 ± 0.1	-176.2 ± 1.3	11.1 ± 1.5	470 ± 51	-76 ± 31	0.65 ± 0.07	-0.10 ± 0.04
	6	28	2.03	-161.7	2.64	684 ± 27	3.1 ± 0.1	-159.8 ± 1.6	1.9 ± 1.8	529 ± 51	-110 ± 38	0.83 ± 0.09	-0.17 ± 0.06
	8	19	5.35	172.6	6.94	1577 ± 121	7.1 ± 0.5	150.2 ± 4.3	22.5 ± 4.5	-431 ± 250	-257 ± 259	-0.29 ± 0.17	-0.17 ± 0.18
	10	21	1.56	-164.3	2.02	1002 ± 61	4.5 ± 0.3	-166.1 ± 1.6	1.9 ± 1.8	285 ± 183	-130 ± 87	0.30 ± 0.20	-0.14 ± 0.09
	11	19	3.76	-175.9	4.87	2042 ± 50	9.2 ± 0.2	161.4 ± 1.4	22.6 ± 1.6	432 ± 112	-819 ± 107	0.23 ± 0.06	-0.43 ± 0.06
	12	16	2.83	-165.1	3.67	1234 ± 57	5.6 ± 0.3	-169.6 ± 1.1	4.5 ± 1.2	144 ± 131	-136 ± 47	0.13 ± 0.11	-0.12 ± 0.04
	13	13	2.29	-166.7	2.97	1082 ± 38	4.9 ± 0.2	-164.5 ± 1.1	2.2 ± 1.2	122 ± 100	2 ± 55	0.12 ± 0.10	0.00 ± 0.05
	16	16	2.39	-174.0	3.10	904 ± 28	4.1 ± 0.1	-167.8 ± 1.1	6.2 ± 1.1	460 ± 64	-46 ± 38	0.54 ± 0.08	-0.05 ± 0.05
	19	14	2.41	-174.0	3.12	1557 ± 94	7.0 ± 0.4	-172.5 ± 1.2	1.5 ± 1.2	-476 ± 557	100 ± 195	-0.33 ± 0.38	0.07 ± 0.13
	24	20	1.51	-167.5	1.95	458 ± 36	2.1 ± 0.2	-179.4 ± 2.3	12.0 ± 2.4	-168 ± 112	-4 ± 61	-0.39 ± 0.26	-0.01 ± 0.14
2201+171	5	11	8.20	50.2	67.10	319 ± 25	17.7 ± 1.4	67.0 ± 4.4	16.8 ± 4.4	145 ± 40	14 ± 38	0.94 ± 0.27	0.09 ± 0.25
2201+315	1	21	5.47	-135.6	23.89	324 ± 7	6.0 ± 0.1	-132.4 ± 1.1	3.2 ± 1.2	-4 ± 3	-6 ± 3	-0.02 ± 0.01	-0.02 ± 0.01
	2	14	3.82	-142.7	16.68	338 ± 7	6.2 ± 0.1	-137.0 ± 1.2	5.7 ± 1.3	-15 ± 5	8 ± 5	-0.06 ± 0.02	0.03 ± 0.02
	4	16	3.43	-140.7	14.97	377 ± 11	6.9 ± 0.2	-135.6 ± 1.6	5.1 ± 1.8	-4 ± 6	6 ± 6	-0.01 ± 0.02	0.02 ± 0.02
	5	10	1.80	-148.9	7.86	332 ± 14	6.1 ± 0.3	-145.3 ± 2.5	3.6 ± 2.7	20 ± 12	20 ± 10	0.08 ± 0.05	0.08 ± 0.04
	6	13	2.00	-147.1	8.76	449 ± 5	8.3 ± 0.1	-145.7 ± 0.6	1.4 ± 0.7	28 ± 5	18 ± 4	0.08 ± 0.01	0.05 ± 0.01
2223-052	1	14	5.28	97.7	44.87	224 ± 19	15.0 ± 1.3	89.2 ± 3.2	8.4 ± 3.2	27 ± 21	-7 ± 15	0.29 ± 0.22	-0.08 ± 0.16
	2	26	3.31	103.4	28.14	126 ± 10	8.4 ± 0.6	99.5 ± 2.2	3.8 ± 2.3	7 ± 4	5 ± 2	0.13 ± 0.08	0.09 ± 0.04
	4	22	1.15	96.1	9.77	305 ± 10	20.3 ± 0.6	111.2 ± 1.4	15.1 ± 1.9	23 ± 7	10 ± 5	0.18 ± 0.06	0.08 ± 0.04
	5	14	0.96	101.4	8.17	218 ± 7	14.5 ± 0.5	94.3 ± 1.6	7.2 ± 2.0	3 ± 6	6 ± 5	0.03 ± 0.07	0.06 ± 0.06
2230+114	2	31	11.22	157.7	91.04	160 ± 11	8.6 ± 0.6	148.4 ± 4.2	9.3 ± 4.2	-6 ± 6	1 ± 6	-0.07 ± 0.07	0.02 ± 0.08
	4	31	6.21	155.5	50.34	26 ± 3	1.4 ± 0.1	-22.1 ± 4.9	177.6 ± 4.9	0 ± 2	3 ± 1	0.01 ± 0.12	0.23 ± 0.11

Table 1 — *Continued*

Source (1)	I.D. (2)	N (3)	$\langle R \rangle$ (mas) (4)	$\langle \theta \rangle$ (deg.) (5)	$d_{proj}$ (pc) (6)	$\mu$ ( $\mu\text{as yr}^{-1}$ ) (7)	$\beta_{obs}$ (8)	$\phi$ (deg.) (9)	$ \langle \theta \rangle - \phi $ (deg.) (10)	$\dot{\mu}_{  }$ ( $\mu\text{as yr}^{-2}$ ) (11)	$\dot{\mu}_{\perp}$ ( $\mu\text{as yr}^{-2}$ ) (12)	$\dot{\eta}_{  }$ ( $\text{yr}^{-1}$ ) (13)	$\dot{\eta}_{\perp}$ ( $\text{yr}^{-1}$ ) (14)
2243-123	2	12	3.65	19.9	24.94	$144 \pm 5$	$5.2 \pm 0.2$	$36.6 \pm 2.1$	$16.8 \pm 2.1$	$-1 \pm 3$	$0 \pm 3$	$-0.01 \pm 0.03$	$0.01 \pm 0.03$
	3	12	1.94	-0.8	13.28	$125 \pm 7$	$4.6 \pm 0.2$	$9.8 \pm 0.8$	$10.6 \pm 0.8$	$6 \pm 4$	$3 \pm 1$	$0.08 \pm 0.05$	$0.04 \pm 0.01$
2251+158	2	78	5.99	-80.2	46.14	$85 \pm 3$	$4.0 \pm 0.1$	$-43.7 \pm 2.1$	$36.5 \pm 2.1$	$1 \pm 1$	$-3 \pm 1$	$0.01 \pm 0.03$	$-0.07 \pm 0.03$
	3	37	2.73	-81.6	21.04	$204 \pm 9$	$9.5 \pm 0.4$	$-52.5 \pm 2.7$	$29.1 \pm 2.7$	$-0 \pm 14$	$18 \pm 15$	$-0.00 \pm 0.12$	$0.17 \pm 0.14$
	4	44	2.70	-106.5	20.77	$286 \pm 6$	$13.4 \pm 0.3$	$-89.2 \pm 1.4$	$17.3 \pm 1.4$	$-58 \pm 7$	$30 \pm 8$	$-0.38 \pm 0.05$	$0.19 \pm 0.05$
	5	61	2.00	-43.3	15.44	$198 \pm 9$	$9.3 \pm 0.4$	$-77.5 \pm 2.1$	$34.3 \pm 2.2$	$-0 \pm 6$	$-24 \pm 5$	$-0.00 \pm 0.06$	$-0.23 \pm 0.05$
	8	23	0.57	-91.2	4.40	$295 \pm 10$	$13.8 \pm 0.5$	$-98.3 \pm 0.9$	$7.2 \pm 0.9$	$-122 \pm 38$	$-81 \pm 16$	$-0.77 \pm 0.24$	$-0.51 \pm 0.10$
2345-167	3	10	1.68	123.3	10.99	$341 \pm 23$	$11.5 \pm 0.8$	$122.8 \pm 3.5$	$0.5 \pm 3.8$	$4 \pm 27$	$-5 \pm 25$	$0.02 \pm 0.13$	$-0.02 \pm 0.12$
	4	15	1.44	120.5	9.45	$276 \pm 8$	$9.3 \pm 0.3$	$121.9 \pm 1.8$	$1.4 \pm 1.9$	$-38 \pm 9$	$10 \pm 10$	$-0.22 \pm 0.05$	$0.06 \pm 0.06$
2351+456	4	13	1.00	-67.4	8.48	$170 \pm 12$	$14.0 \pm 1.0$	$-73.3 \pm 4.2$	$5.9 \pm 4.6$	$-9 \pm 9$	$19 \pm 9$	$-0.15 \pm 0.15$	$0.33 \pm 0.17$
	5	10	0.67	-96.7	5.67	$132 \pm 12$	$10.9 \pm 1.0$	$-76.6 \pm 3.3$	$20.0 \pm 3.6$	$4 \pm 10$	$23 \pm 6$	$0.08 \pm 0.23$	$0.53 \pm 0.15$

**Note.** — Columns are as follows: (1) Source name in B1950 coordinates; (2) Component ID; (3) Number of epochs; (4) Mean radial separation from core in milli-arcseconds (averaged over all epochs); (5) Mean structural position angle in degrees; (6) Mean projected radial distance in parsecs; (7) Angular proper motion in micro-arcseconds per year; (8) Apparent speed in units of the speed of light; (9) Proper motion position angle in degrees; (10) Absolute difference between mean structural position angle and proper motion position angle in degrees; (11) Angular acceleration parallel to the proper motion position angle in micro-arcseconds per year per year; (12) Angular acceleration perpendicular to the proper motion position angle in micro-arcseconds per year per year; (13) Relative parallel acceleration as defined in §3; (14) Relative perpendicular acceleration as defined in §3;